bioRxiv preprint doi: https://doi.org/10.1101/2022.08.11.503144; this version posted July 29, 2023. The copyright holder for this preprint (which was not certified by peer review) is the author/funder, who has granted bioRxiv a license to display the preprint in perpetuity. It is made available under aCC-BY-NC 4.0 International license.

Modeling and Simulation of Neocortical Micro- and Mesocircuitry. Part I: Anatomy

Michael W. Reimann[1,8,†], Sirio Bolaños-Puchet[1,8], Jean-Denis Courcol[1,8], Daniela Egas Santander[1,8], Alexis Arnaudon[1], Benoît Coste[1], Fabien Delalondre[1], Thomas Delemontex[1], Adrien Devresse[1], Hugo Dictus[1], Alexander Dietz[1], András Ecker[1], Cyrille Favreau[1], Gianluca Ficarelli[1], Mike Gevaert[1], Joni Herttuainen[1], James B. Isbister[1], Lida Kanari[1], Daniel Keller[1], James King[1], Pramod Kumbhar[1], Samuel Lapere[1], Jānis Lazovskis[3], Huanxiang Lu[1], Nicolas Ninin[1], Fernando Pereira[1], Judit Planas[1], Christoph Pokorny[1], Juan Luis Riquelme[1], Armando Romani[1], Ying Shi[1], Jason P. Smith[4], Vishal Sood[1], Mohit Srivastava[5], Werner Van Geit[1], Liesbeth Vanherpe[1], Matthias Wolf[1], Ran Levi[6,9], Kathryn Hess[7,9], Felix Schürmann[1,9], Eilif B. Muller[1,9], Srikanth Ramaswamy[1,2,9,†], and Henry Markram[1,9,†]

[1]Blue Brain Project, École polytechnique fédérale de Lausanne (EPFL), Campus Biotech, Geneva, Switzerland
[2]Neural Circuits Laboratory, Newcastle University, UK
[3]Riga Business School, Riga Technical University, Riga, Latvia
[4]Nottingham Trent University, Nottingham, UK
[5]ELKH-University of Debrecen, Neuroscience Research Group, Hungary
[6]University of Aberdeen, Aberdeen, UK
[7]Laboratory for Topology and Neuroscience (UPHESS), Brain Mind Institute, School of Life Sciences, École polytechnique fédérale de Lausanne (EPFL), Lausanne, Switzerland
[8]Co-lead authors
[9]Co-senior authors
[†]Corresponding authors

July 29, 2023

bioRxiv preprint doi: https://doi.org/10.1101/2022.08.11.503144; this version posted July 29, 2023. The copyright holder for this preprint (which was not certified by peer review) is the author/funder, who has granted bioRxiv a license to display the preprint in perpetuity. It is made available under aCC-BY-NC 4.0 International license.

Abstract

The function of the neocortex is fundamentally determined by its repeating microcircuit motif, but also by its rich, interregional connectivity. We present a data-driven computational model of the anatomy of non-barrel primary somatosensory cortex of juvenile rat, integrating whole-brain scale data while providing cellular and subcellular specificity. The model consists of 4.2 million morphologically detailed neurons, placed in a digital brain atlas. They are connected by 14.2 billion synapses, comprising local, long-range and extrinsic connectivity. We delineated the limits of determining connectivity from anatomy, finding that it reproduces the targeting of PV+ and VIP+ interneurons only with explicitly added specificity, but the one of Sst+ neurons even without. Globally, connectivity was characterized by local clusters tied together through hub neurons in layer 5, demonstrating how local and interegional connectivity are complicit, inseparable networks. A 211,712 neuron subvolume of the model has been made freely and openly available to the community.

bioRxiv preprint doi: https://doi.org/10.1101/2022.08.11.503144; this version posted July 29, 2023. The copyright holder for this preprint (which was not certified by peer review) is the author/funder, who has granted bioRxiv a license to display the preprint in perpetuity. It is made available under aCC-BY-NC 4.0 International license.

1 Introduction

Cortical dynamics underlie many cognitive processes and emerge from complex multi-scale interactions. These emerging dynamics can be explored in *large-scale, data-driven, biophysically-detailed* models (Markram et al., 2015; Billeh et al., 2020), which integrate different levels of organization. The strict biological and spatial context enables the integration of knowledge and theories, the testing and generation of precise hypotheses, and the opportunity to recreate and extend diverse laboratory experiments within a single model. This approach differs from more abstract models in that it emphasizes *anatomical completeness* of a chosen brain volume rather than implementing a specific hypothesis. Using a "bottom-up" modelling approach, many detailed constituent models are combined to produce a larger, multi-scale model. To the best possible approximation, such models should explicitly include different cell and synapse types with the same quantities, geometric configuration and connectivity patterns as the biological tissue it represents.

Investigating the multi-scale interactions that shape perception requires a model of multiple cortical subsregions with inter-region connectivity, but it also requires the subcellular resolution provided by a morphologically detailed model. In particular, Barabási et al., 2023 argued that the function of the healthy or diseased brain can only be understood when the true physical nature of neurons is taken into account and no longer simplified into point-neuron networks. In that regard, modern electron-microscopic datasets have reached a scale that allows the reconstruction of a ground truth wiring diagram of local connectivity between several hundred neurons. However, this only covers a small fraction of inputs a cortical neuron receives. While afferents from outside the reconstructed volume are detected, one can only speculate about the identity of their source neurons and connections between them. The scale required to understand inter-regional interactions is only available at lower resolutions in the form of region-to-region or voxel-to-voxel connectivity data.

To help better understand cortical structure and function, we present a general approach to create morphologically detailed models of multiple interconnected cortical regions based on the geometry of a digitized volumetric brain atlas, and including synaptic connectivity predicted from anatomy and biological constraints (Figure 1). We used it to build a model of the juvenile rat non-barrel somatosensory (nbS1) regions (Figure 1, center). The workflow is based on the work described in Markram et al. (2015), with several additions, refinements and new data sources that have been independently described and validated in separate publications (Table 1). The model captures the morphological diversity of neurons and their placement in the actual geometry of the modeled regions through the use of voxel atlas information in each step. We calculated at each point represented in the atlas the distance to and direction towards the cortical surface (Figure 1; step 1). We used that information to select from a pool of morphological reconstructions anatomically fitting ones and orient their dendrites and axons appropriately (Figure 1; step 2). As a result, the model was anatomically complete in terms of the volume occupied by dendrites in individual layers. We then combined established algorithms for the prediction of local (Reimann et al., 2015) and long-range (Reimann et al., 2019) connectivity (Figure 1; step 3) as well as extrinsic connectivity from thalamic sources (Markram et al., 2015, (Figure 1; step 4) to generate a connectome combining those scales, and at subcellular resolution.

The model is to our knowledge the first model combining local with long-range connectivity while taking the actual shape of the modeled regions into account, allowing us to determine the limits of anatomy-based predictions of connectivity. The connectome has been theorized to be derivable from anatomy, specifically the locations and densities of neuronal processes (Peters and Feldman, 1976; Garey, 1999). While this approach is powerful (Reimann et al., 2015; Gal et al., 2017; Reimann et al., 2017b) it remains unclear to what degree it can recreate the targeting of specific postsynaptic compartments (Tremblay et al., 2016) found in certain inhibitory pathways (see Mishchenko et al., 2010 contrasting Hill et al., 2012). The availability of increasingly large electron-microscopic datasets, such as MICrONS (MICrONS-Consortium et al., 2021), enabled us to systematically compare our model to their results, and thereby uncover the strength and nature of the targeting mechanisms shaping connectivity beyond neuronal and regional anatomy.

bioRxiv preprint doi: https://doi.org/10.1101/2022.08.11.503144; this version posted July 29, 2023. The copyright holder for this preprint (which was not certified by peer review) is the author/funder, who has granted bioRxiv a license to display the preprint in perpetuity. It is made available under aCC-BY-NC 4.0 International license.

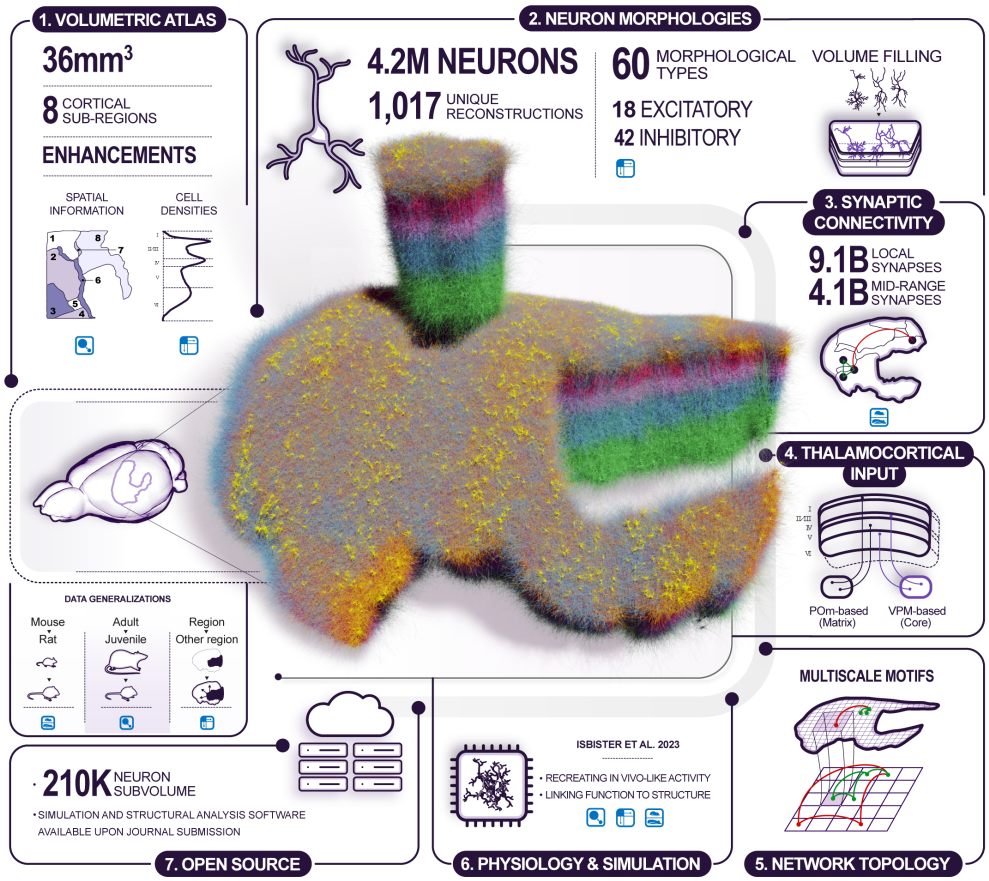

Figure 1: Overview of the model building and analysis workflow. Step 1: Building was based on a volumetric atlas of the modeled regions: (1) S1J; (2) S1FL; (3) S1Tr; (4) S1HL; (5) S1Sh; (6) S1DZ; (7) S1DZO; (8) S1ULp. Additional atlases of biological cell densities and local orientation towards the surface were built. Step 2: Neuron morphologies were reconstructed and classified into 60 morphological types (*m-types*). They were placed in the volume according to the densities and orientations from step 1. Step 3: The anatomy of intrinsic synaptic connectivity was derived as the union of one algorithm for *local* connectivity and one for *long-range* connectivity. Step 4: Extrinsic inputs from two thalamic sources were placed on modeled dendrites according to published methods. Step 5: Taken together, these steps allowed us to predict the topology of connectivity at scale with (sub-)cellular resolution. Step 6: The anatomical model served as the basis of a physiological model, ready to be simulated. This is presented in an accompanying manuscript. Step 7: The model, simulation and analysis tools have been made publicly available. Left: During modeling, three types of generalization had to be made to fulfill input data requirements: from mouse to rat, from adult to juvenile, and from one cortical region to another. Generalizations used are indicated in each step.

bioRxiv preprint doi: https://doi.org/10.1101/2022.08.11.503144; this version posted July 29, 2023. The copyright holder for this preprint (which was not certified by peer review) is the author/funder, who has granted bioRxiv a license to display the preprint in perpetuity. It is made available under aCC-BY-NC 4.0 International license.

We found that the distribution of postsynaptic compartments targeted by connections from somatostatin (Sst)-positive neurons is readily predicted from anatomy only, while for parvalbumin (PV)-positive and vasoactive intestinal peptide (VIP)-positive neurons additional specificity plays a role. We found no indication of additional specificity for excitatory neurons.

Additionally, we characterized several aspects of connectivity that do emerge from anatomical constraints (Figure 1; step 5). First, we predicted the impact of brain geometry, specifically the biological variability of brain geometry between regions, on the topology of connectivity. We found that differences in cortical thickness and curvature have surprisingly large effects on how much individual layers contribute to the connections a neuron partakes in. Second we characterized the predicted structure of connectivity at an unprecedented scale and determine its implications for neuronal function. In particular, we analyzed how the widths of thalamo-cortical axons constrains the types of cortical maps emerging; we characterized the global topology of interacting local and long-range connectivity; we found a highly complex topology of local and long-range connectivity that specifically requires neuronal morphologies; We characterized highly connected clusters of neurons, distributed throughout the volume that are tied together by long-range synaptic paths mediated by neurons in layer 5, which act as "highway hubs" interconnecting spatially distant neurons in the model.

Finally, we present an accompanying manuscript that details neuronal and synaptic physiology modeled on top of these results, describes the emergence of an *in vivo*-like state of simulated activity, and delivers a number of *in silico* experiments generating insights about the neuronal mechanisms underlying published *in vivo* and *in vitro* experiments (Figure 1; step 6). In the spirit of open science and to accelerate its refinement, we have made the model and simulation and analysis tools openly available to the community (Figure 1; step 7).

Table 1: References to publications of input data and methods employed for individual modeling steps. An asterisk next to a reference indicates that substantial adaptations or refinements of the data or methods have been performed that will be explained in this manuscript. In the other cases, a basic summary will be provided and an exhaustive description in the STAR*Methods.

	Data	
Stage	**Topic**	**Reference**
Atlasing	Region annotation atlas	Paxinos and Watson (2007)
	Orientation, depth and flat map	Bolaños-Puchet and Reimann (prep)
	Cell density profiles	Keller et al. (2019)
Volume filling	Neuron reconstructions	Markram et al. (2015)
	in vivo neuron reconstructions	*New, original data
Synaptic connectivity	Bouton densities and numbers of synapses per connection	Reimann et al. (2015)
	Pathway strengths, synapse density profiles and topographical mapping	*Reimann et al. (2019)
Thalamic inputs	Bouton density profiles	Meyer et al. (2010)
	Projection axon lengths and widths	Economo et al. (2016)
	Modeling methods	
Stage	**Topic**	**Reference**
Atlasing	Cell density volume generation	Keller et al. (2019)
Volume filling	Neuron classification	Kanari et al. (2019)
	Neuron placement	*Markram et al. (2015)
Synaptic connectivity	Local connectivity	Reimann et al. (2015)
	Inter-region connectivity	Reimann et al. (2019)
Thalamic inputs	Input generation	*Markram et al. (2015)

bioRxiv preprint doi: https://doi.org/10.1101/2022.08.11.503144; this version posted July 29, 2023. The copyright holder for this preprint (which was not certified by peer review) is the author/funder, who has granted bioRxiv a license to display the preprint in perpetuity. It is made available under aCC-BY-NC 4.0 International license.

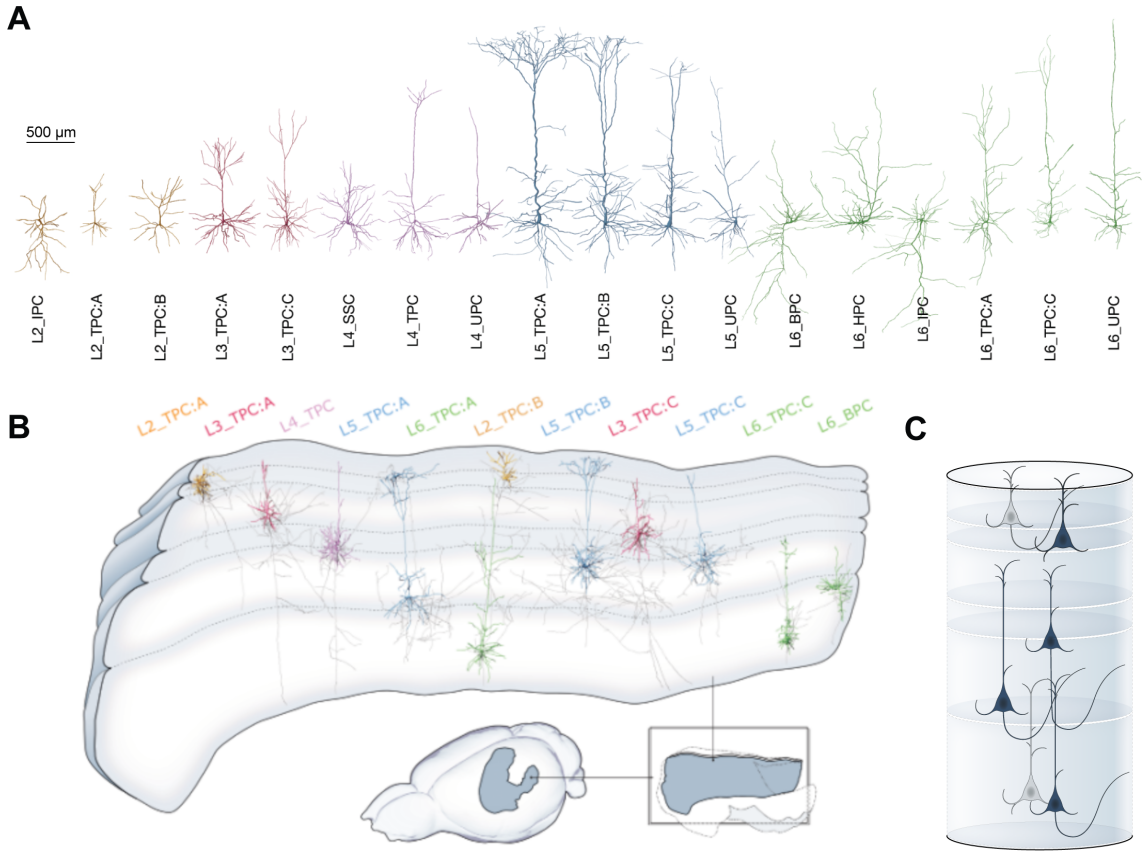

Figure 2: Anatomy of the model A: Modeled brain regions (solid colors) in the context of the non-modeled somatosensory regions (transparent). Derived from (Paxinos and Watson, 2007). B: Modeled cortical layers in the context of the entire brain, with exemplars of excitatory morphological types placed in the model. C: The placement of each morphological type recreates the biological laminar anatomy of dendrites and axons, which then serves as the basis of local connectivity.

2 Results

2.1 Atlas-based neuron placement

The workflow for modeling the anatomy of juvenile rat nbS1 is based on the work described in Markram et al. (2015), with several additions and refinements. Most of the individual steps and data sources have already been independently described and validated in separate publications (Table 1). Basis of the work was a digital atlas of juvenile rat somatosensory cortex, based on the classic work of Paxinos and Watson (2007) (Figure1, step 1.). The atlas provides region annotations, i.e., each voxel is labeled by the somatosensory subregion it belongs to. It also provided a spatial context for the model, with the non-modeled barrel region being surrounded on three sides by modeled regions (specifically: S1DZ and S1ULp). The atlas was enhanced with spatial data on cortical depth and local orientation towards the cortical surface (Bolaños-Puchet and Reimann, prep). We further added annotations for cortical layers, placing layer boundaries at fixed normalized depths (Table S2). Using laminar profiles of cell densities (Keller et al., 2019), we generated additional voxelized datasets with cell densities for each morphological type (see STAR*Methods).

Next, we filled the modeled volume of the atlas with neurons (Figure 1, step 2.). Neuronal morphologies were reconstructed, either *in vivo* or in slices, and repaired algorithmically (Anwar et al., 2009; Markram et al., 2015). Out of 1017 morphologies, 58 were new *in vivo* reconstructions used for the first time in this work (see STAR*Methods). The morphologies were classified into 60

bioRxiv preprint doi: https://doi.org/10.1101/2022.08.11.503144; this version posted July 29, 2023. The copyright holder for this preprint (which was not certified by peer review) is the author/funder, who has granted bioRxiv a license to display the preprint in perpetuity. It is made available under aCC-BY-NC 4.0 International license.

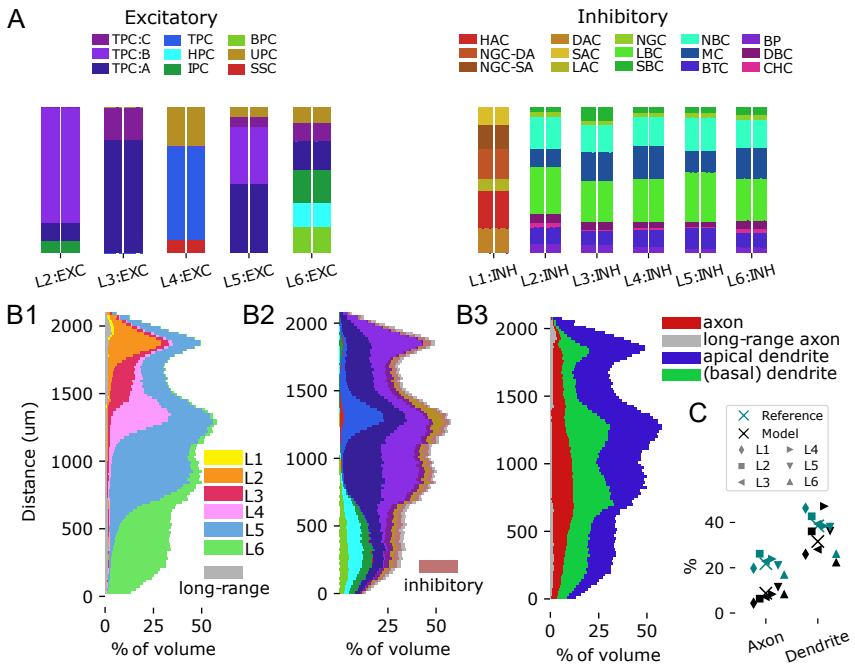

Figure 3: Volumetric anatomy of the model A: M-type composition per layer: For each layer, stacked histograms of the relative fractions of each m-type, comparing the model (right bar for each layer) to the input data (left bar). For simplicity, the layer designation is stripped from each m-type. Left: For excitatory types; right: Inhibitory types. B: Stacked histograms of the fraction of space filled by neurites at various depths in the model. The y-axis indicates the distance in μm from the bottom of layer 6. B1: For neurites of neurons in different layers indicated in different colors. Grey: estimated lower bound for the volume of axons supporting the long-range connectivity. B2: For neurites of different m-types. Colors as in C, but inhibitory types are grouped together. B3: For different types of neurites. C: Comparing fractions for axons and dendrites to the literature (Santuy et al., 2018). X-marks indicate overall means, other marks means in individual layers; teal: reference, black: model.

morphological types (*m-types*, Table S1; 18 excitatory, 42 inhibitory; Figure 2), based on expert knowledge and objectively confirmed by topological classification (Kanari et al., 2019).

As only 58 morphologies were *in vivo* reconstructions, the rest potentially suffered from slicing artifacts, despite applying a repair algorithm (Markram et al., 2015). A topological comparison (Kanari et al., 2018, 2019) between axons and dendrites of neurons in all layers (Fig. S4) revealed that in vitro reconstructions from slices could not capture detailed axonal properties beyond 1000 μm, but could faithfully reproduce dendritic arborization.

Cell bodies for all m-types were placed in atlas space according to their prescribed cell densities. At each soma location, a reconstruction of the corresponding m-type was chosen based on the size and shape of its dendritic and axonal trees (Figure S6). Additionally, it was rotated to according to the orientation towards the cortical surface at that point. These steps ensured that manually identified features of the morphologies (Table S3) landed in the correct layers (Figure 2B, C; S7).

2.2 Biological dendrite volume fractions emerge in the model

The distribution over 60 m-types in the model captured the great morphological diversity of cortical neurons and matched the reference data used (Figure 3A, see STAR*Methods). The placement of morphological reconstructions matched expectation, showing an appropriately layered structure with only small parts of neurites leaving the modeled volume (Figure 2D, E). For a more quantitative validation, we calculated the fraction of the volume occupied by neurites in 100 depth bins of a cylindrical volume spanning all layers and with a radius of 100 μm (Figure 3B). This included an estimated volume for axons forming the long-range connectivity between modeled regions, based

bioRxiv preprint doi: https://doi.org/10.1101/2022.08.11.503144; this version posted July 29, 2023. The copyright holder for this preprint (which was not certified by peer review) is the author/funder, who has granted bioRxiv a license to display the preprint in perpetuity. It is made available under aCC-BY-NC 4.0 International license.

on its synapse count (see below and STAR*Methods).

We found a clearly layered structure also for the neurite volumes, with apical dendrites contributing substantially to the volume in layers above their somas. The volume was clearly dominated by dendrites, filling between 23% and 47% of the space, compared to 2% to 11% for axons (Figure 3D3). The range of values for dendrites matched literature closely (between 26% and 46%, Santuy et al., 2018). Conversely, values for axons were lower than literature (between 17% and 24%); however, this is explained by the vast amount of external input axons from non-somatosensory and extracortical sources that are not part of the model.

2.3 Local, long-range and extrinsic connectivity modeled separately

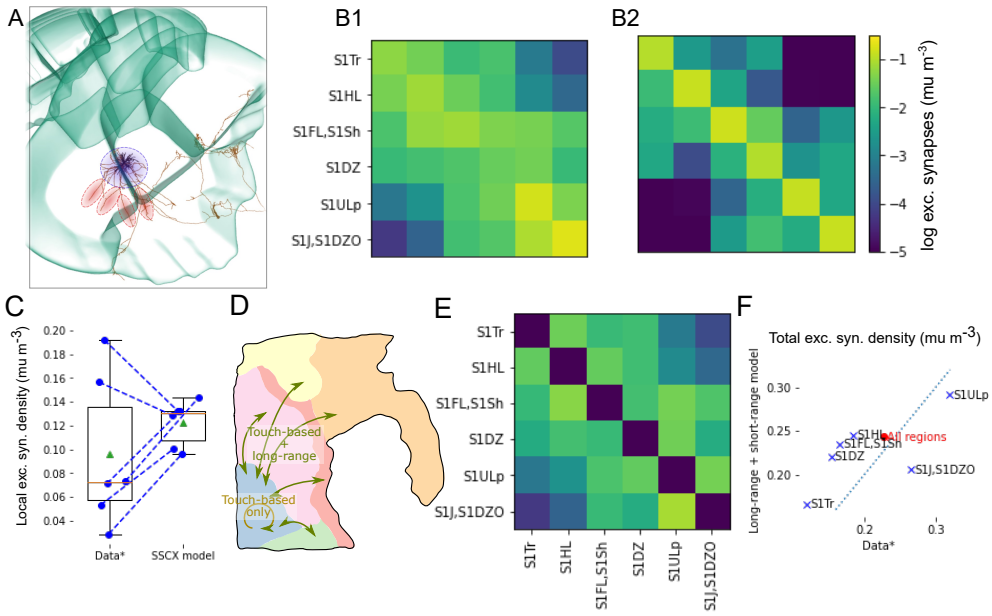

Figure 4: Intrinsic connectivity as union of local and long-range connectivity. A: An exemplary layer 5 PC axon reconstruction shown in the context of mouse somatosensory regions, rendered in the Janelia MouseLight neuron browser (mouselight.janelia.org, Gerfen et al. (2018)). The blue circle highlights local branches all around the soma. Red highlights depict more targeted collaterals into neighboring regions. B1: Predicted pathway strengths as indicated in Figure S2C3. B2: Pathway strength emerging from the application of the apposition-based connectivity algorithm described in Reimann et al. (2015). C: Values of the diagonal of (B1) compared to the diagonal of (B2). D: Schematic of the strategy for connectivity derivation: Within a region only apposition-based connectivity is used; across regions the union of apposition-based and long-range connectivity. E: Connection strength constraints for the long-range connectivity derived by subtracting B2 from B1 and setting elements < 0 to 0 (colors as in B). F: Resulting total density from both types of modeled synaptic connections in individual regions compared to the data in (B1).

Synaptic connections were placed in the model using a previously published approach (Reimann et al., 2015) that selects synapses as a subset of axo-dendritic, axo-somatic and axo-axonic appositions, based on biologically motivated rules (Figure 1, step 3.). However, according to our analysis of the morphologies used, most axons were only accurately reconstructed up to 1000μm from the soma (see above). This contrast between local axon around the soma and more long-range collaterals stretching into neighboring regions can also be seen in *in vivo* reconstructions (Fig. 4A). Therefore, to model connections at larger distances, we used a second, previously published algorithm (Reimann et al., 2019). It places long-range synapses according to three biological principles that all need to be separately parameterized: First, connection strength: ensuring that the total number of synapses in a region-to-region pathway matches biology. Second, layer profiles: ensur-

bioRxiv preprint doi: https://doi.org/10.1101/2022.08.11.503144; this version posted July 29, 2023. The copyright holder for this preprint (which was not certified by peer review) is the author/funder, who has granted bioRxiv a license to display the preprint in perpetuity. It is made available under aCC-BY-NC 4.0 International license.

ing that the relative number of synapses in different layers matches biology. Third, topographical mapping: Ensuring that the specific locations within a region targeted by long-range connections of neurons describe a biologically parameterized, topographical mapping. We note that in the literature on macro-scale connectomics, the pathways between somatosensory regions would be considered "short-range, inter-regional connections". We will still refer to connections from the two algorithms as the *local* and *long-range* connectomes respectively, for simplicity and because of the intuitive contrast it invokes.

To parameterize connection strengths, we used data provided by the Allen Institute (Harris et al., 2019), adapted from mouse to rat, yielding expected densities of projection synapses between pairs of regions (Figure 4B1). First, we addressed the question of to what degree the local connectome algorithm suffices to model the connectivity within a region. To that end, we compared the mean excitatory synapse densities of local connectivity to the target values adapted from (Reimann et al. (2019), Figure 4B1 vs. B2; C). We found that the overall average matches the data fairly well, however the variability across regions was lower in the model ($0.123 \pm 0.017\,\mu m^{-1}$; mean $\pm$ std in the model vs. $0.097 \pm 0.06\,\mu m^{-1}$). Based on these results, we decided that the local connectome sufficed to model connectivity within a region. It also created a number of connections across region borders (Figure 4B2). Consequently, we parameterized the strengths of additional long-range connections to be placed as the difference between the total strength from the data and the strengths resulting from local connectivity, with connection strengths within a region set to zero (Figure 4E). As a result synaptic connections between neighboring regions will be placed by both algorithms (Figure 4D), with a split ranging from 20% local to 70% local. The lower spread of apposition-based synapse density within a region (see above) will also reduce the variability of combined synapse density from both algorithms (Figure 4F). While this will halve the coefficient of variation of density across regions from 0.34 to 0.17, the overall mean density over all regions is largely preserved (0.23 data vs. 0.24 for the combined algorithms; Figure 4F, red dot).

Finally, the dendritic locations of synaptic inputs from thalamic sources were modeled as in (Markram et al., 2015), using experimental data on layer profiles of bouton densities of thalamo-cortical axons, and morphological reconstructions of these types of axons (Figure 1, step 4; S9A; STAR*Methods). Based on these data, each thalamic input fiber was assigned an innervated domain in the model, recreating the layer profile along an axis orthogonal to layer boundaries and spreading equally in the other dimensions (Fig. S9B-E). We modeled two types of thalamic inputs, based on the inputs into barrel cortex from the ventral posteromedial nucleus (VPM-based) and from the posterior medial nucleus (POm-based) respectively (Harris et al., 2019; Shepherd and Yamawaki, 2021). While barrel cortex was not a part of the model, we used these projections as examples of a *core*-type projection, providing feed-forward sensory input (VPM-based) and a *matrix*-type projection, providing higher-order information (POm-based).

The numbers of thalamic input fibers innervating the model were estimated as follows. Laminar synapse density profiles were summed over the volume to estimate the total number of thalamo-cortical synapses, and the number of synapses per neuron was estimated from the lengths of thalamo-cortical axons. The ratio of these numbers resulted in 72,950 fibers for the POm-based matrix-type projection, and 100,000 fibers for the VPM-based core-type projection. These numbers are consistent with the volume ratio of the two thalamic nuclei ($1.25mm^3$ for POm to $1.64mm^3$ for VPM; ratio: 0.76).

2.4 Specificity of axonal targeting

For the axons of various inhibitory neuron types, certain aspects of connection specificity have been characterized (Tremblay et al., 2016), such as a preference for peri-somatic innervation for PV+ basket cells. The local connectivity in the model is based axo-dendritic overlap, combined with a pruning rule that prefers multi-synaptic connections, but does not take the post-synaptic compartment type into account (Reimann et al., 2015). As such, it captures targeting preferences resulting from specific axonal morphologies, but not potential effects due to potential molecular mechanisms during synapse formation or pruning. This is based on the idea that the developmental

bioRxiv preprint doi: https://doi.org/10.1101/2022.08.11.503144; this version posted July 29, 2023. The copyright holder for this preprint (which was not certified by peer review) is the author/funder, who has granted bioRxiv a license to display the preprint in perpetuity. It is made available under aCC-BY-NC 4.0 International license.

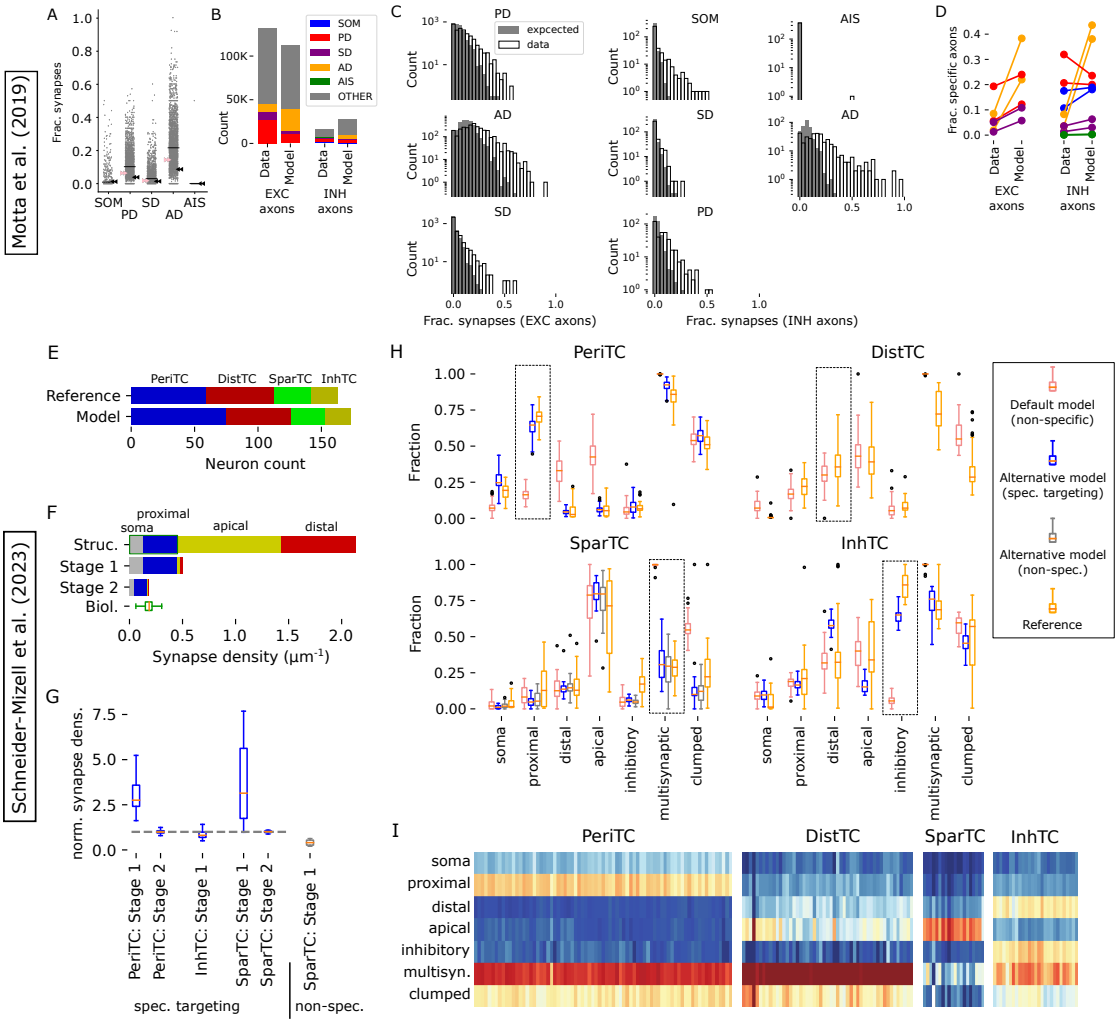

Figure 5: Recreating an electron-microscopic specificity analysis In the top part we analyzed synapses, axons and dendrites in an approximately cubic volume in L4, emulating the techniques of Motta et al., 2019. In the bottom part we analyzed a 100 x 100 μm volume of the MICrONS dataset defined by Schneider-Mizell et al., 2023. A: Fraction of synapses placed on somata (SOM), proximal dendrites (PD), smooth dendrites (SD), apical dendrites (AD) and axon initial segments (AIS) for axon fragments in the sampled volume. Black bars indicate mean values over axons, arrows indicate binomial probabilities fit to observations of axons forming at least a single synapse; pink: for excitatory axons, black: inhibitory. Fractions missing from 100% are onto other compartment types. B: Overall count on synapses on different postsynaptic compartment classes inside the studies volumes, comparing the data of Schneider-Mizell et al., 2023 to the model. Colors as indicated in the legend. C: Distributions of the fractions of synapses onto different compartment types over excitatory (left) and inhibitory (right) axons. Expected from the binomial model in A (grey) against the observations in our anatomical model (black outlines). D: Fraction of axons with significantly increased synapse counts onto different compartment types compared to the binomial control. Indicated for two values of the false detection rate criterion (q=0.05, 0.3, Storey and Tibshirani, 2003). Comparing the reference data to our anatomical model. E: Top numbers of neurons in four connectivity-derived classes in the 100 x 100 μm volume of the MICrONS dataset, defined by Schneider-Mizell et al., 2023. Bottom: Numbers in a comparable volume of the model. For assignment of m-types into the four classes see the main text. F: Derivation of alternative connectivity with targeting specificity, using the example of the "PeriTC" class. The axo-dendritic appositions of an axon (top) are classified as matching the targeting (green box; here: appositions with somata or proximal dendrites) or not. Non-matching appositions are removed with probability p_{nt} (middle). This is followed by a non-specific removal of connections (formed by single or multiple synapses) until the biological density of synapses on the axon is met (bottom).

bioRxiv preprint doi: https://doi.org/10.1101/2022.08.11.503144; this version posted July 29, 2023. The copyright holder for this preprint (which was not certified by peer review) is the author/funder, who has granted bioRxiv a license to display the preprint in perpetuity. It is made available under aCC-BY-NC 4.0 International license.

G: Bouton densities resulting from the process in F. Left to right: For PeriTC neurons, targeting somata and proximal dendrites; for InhTC neurons, targeting inhibitory neurons; for SparTC neurons, targeting the first synapse of a connections; for SparTC neurons, without targeting preference. Respective optimized p_{nt} values reported in the main text. H: Resulting targeting of postsynaptic compartments, fraction of synapses in multisynaptic connections and clumped synapses (see Schneider-Mizell et al., 2023). Red: Default model; blue: optimized alternative model with specific targeting; grey: optimized alternative model without specific targeting; orange: data of Schneider-Mizell et al., 2023 Boxes outline the characteristic feature of each class. I: Inhibitory targeting specificities combining the best performing models.

mechanisms underlying connectivity are manifold and complicated, but their cumulative effect is at least partially visible in the characteristic shapes of the neurites. We have previously demonstrated that this suffices to create highly nonrandom network topologies that match many biological trends (Reimann et al., 2015; Gal et al., 2017; Reimann et al., 2017a), but the analyses have so far been focused mainly on the excitatory sub-network. To investigate to what degree the approach suffices to explain observed targeting trends, we compared the model to characterizations of targeting specificity from the literature, recreating the electron microscopy studies of Motta et al., 2019 and Schneider-Mizell et al., 2023 *in silico*.

Motta et al. (2019) analyzed an approximately 500,000 μm^3 volume of tissue in layer 4, considering the postsynaptic targets of the contained axons. As axons in the volume were fragments, specificity was assessed by comparing the data to a binomial control fit against observations of axons forming at least one synapse onto a postsynaptic compartment type (see STAR*Methods). Axons with unexpectedly high fractions onto a compartment type were then considered to target that type. We calculated targeting fractions of axons forming at least 10 synapses in a comparable layer 4 volume of our model (Figure 5A). Compared to Motta et al. (2019), fractions of synapses onto apical dendrites were elevated, and more inhbititory synapses were considered (Figure 5B). As in the original study, for almost all compartment types, observed distributions were more long tailed than expected with a number of axons showing a significantly high targeting fraction (Figure 5C). The fractions of axons with such specificities also matched the reference, except for an even higher fraction being specific for apical dendrites in the model (Figure 5D). Further analysis (not shown) revealed that this match resulted from local connectivity in our model using the principle of *cooperative synapse formation* (Fares and Stepanyants, 2009), where all synapses forming a connections are kept or pruned together. This creates a statistical dependence between the synapses that results in a significant deviation from the binomial control models. We conclude that the non-random trends observed by Motta et al. (2019) are an indication of cooperative synapse formation captured by our model.

Recently, the MICrONS dataset (MICrONS-Consortium et al., 2021) has been analyzed with respect to the axonal targeting of inhibitory subtypes in a 100 x 100 μm subvolume spanning all layers (Schneider-Mizell et al., 2023). Similar to Motta et al. (2019) they considered their distributions of types of postsynaptic compartments. But due to the larger reconstructed volume, they were able to analyze complete or almost complete axons, allowing for a quantitative comparison rather than relying on a fitted binomial control model. Additionally, they calculated the fraction of synapses that are part of a multisynaptic connections and the fraction thereof that is within 15 μm of another synapse of the same connection.

A comparable volume of the model (see STAR*Methods) contained 173 interneurons vs. 163 in the original study. Their distribution into four connectivity classes according to morphological and molecular determinants hypothesized by Schneider-Mizell et al. (2023) approximately matched as well (Figure 5E; perisomatic targeting: Basket Cells; distal targeting: Sst+; sparsely targeting: Neurogliaform Cells and L1; inhibitory targeting: bipolar and VIP+). The postsynaptically targeted compartments matched for the distal targeting group (Figure 5H, top right; 5I), indicating that their preference can be explained by their axonal morphology, specifically its trend to ascend to and then branch in superficial layers. For the other three classes, their respective eponymous trends were not recreated (Figure 5H, red vs. orange).

bioRxiv preprint doi: https://doi.org/10.1101/2022.08.11.503144; this version posted July 29, 2023. The copyright holder for this preprint (which was not certified by peer review) is the author/funder, who has granted bioRxiv a license to display the preprint in perpetuity. It is made available under aCC-BY-NC 4.0 International license.

We then explored the strengths of targeting mechanisms required to explain postsynaptic targets in a modified version of our connectivity algorithm: Beginning with all axo-dendritic appositions as potential synapses, we first remove appositions that are not placed on the preferred postsynaptic compartment with a probability p_{nt} (Figure 5F; top to middle). This replaces an non-specific, but otherwise identical first pruning steps in the regular version of our algorithm. This is followed by removing connections non-specifically, until the biological density of synapses on the axon is matched (Figure 5F; middle to bottom). As reference for biological densities of synapses on axons, we use the sources listed in Reimann et al. (2015)

For the perisomatic targeting class, probability p_{nt} to remove non-proximal, non-soma synapses was optimized against the data of Schneider-Mizell et al. (2023) to 97%. The remaining synapses had a density on the axons of perisomatic targeting cells that was three times higher than biology, which could be reduced in the second, non-specific pruning step removing two thirds of the connections (Figure 5G, left). This indicates substantial room for rewiring through structural plasticity while preserving the targeting specificity of perisomatic targeting cells. The resulting specificity of postsynaptic compartments and multi-synaptic connections then match the reference data (Figure 5H, top left, blue vs orange; 5I).

For the inhibitory targeting class, probability p_{nt} to remove synapses on non-inhibitory neurons was optimized to the a similar value of 96.5%. Curiously, this first step already reduced the resulting axonal density of synapses to the biological value, indicating that this class of interneurons cannot perform substantial rewiring without losing its targeting specificity (Figure 5G, second from left).

For sparsely targeting cells, we evaluated two hypotheses: First, we note that this targeting class is associated with Neurogliaform Cells, which are known to have volumetrically transmitting synapses. It is possible that the sparseness of their targeting can be explained by very few of their synapes having an anatomical postsynaptic partner, rather than by a targeting mechanism. Indeed a non-specific removal of 96% of all synapses recreated the sparsity of these connections found in Schneider-Mizell et al. (2023) (Figure 5H, bottom left, grey vs orange; 5I). This reduced the axonal density of synapses to 30% of the biological value, implying that the remaining 70% may be volumetrically transmitting (Figure 5G, right). Second, we randomly picked a "first" synapse from each connection formed by this class that we considered to be targeted. Of the remaining synapses, we removed $p_{nt} = 95\%$, which recreated the characteristic sparsity of the connections equally well (Figure 5H, bottom left, blue vs orange; 5I). In this case, the second, non-specific pruning step was required, indicating substantial room for rewiring (Figure 5G, second from right).

2.5 Structure of thalamic inputs

Though we have found that the anatomy-based prediction of connectivity underestimates the specificity of some inhibitory connection types, it remains a powerful tool that has been demonstrated to recreate non-random trends of excitatory connections that make up the majority of synapses (Reimann et al., 2015, 2017b; Gal et al., 2017). We therefore set out to characterize the anatomy and topology of connections at all scales considered in the model. We began with the thalamic input connections. Anatomical factors affecting this pathway were: On the presynaptic side, average statistics of thalamic axons in the form of their horizontal spread and laminar synapse density profiles. On the postsynaptic side, individual dendritic morphologies, cell placement and orientation.

Regarding the laminar structure, we found for both projections that the peaks of the mean number of thalamic inputs per neuron occur at lower depths than the peaks of the synaptic density profiles (Figure 6A). This is consistent with synapses on apical dendrites of PCs being higher than their somas, but the fact that most peaks occur at places where the synapse density is close to zero gives a clear indication that synapse density profiles alone can be misleading about the location of innervated neurons. At the level of individual neurons, the number of thalamic inputs varied greatly, even within the same layer (Figure 6B). Overall, the matrix-type projection innervated

bioRxiv preprint doi: https://doi.org/10.1101/2022.08.11.503144; this version posted July 29, 2023. The copyright holder for this preprint (which was not certified by peer review) is the author/funder, who has granted bioRxiv a license to display the preprint in perpetuity. It is made available under aCC-BY-NC 4.0 International license.

neurons in layers 1 and 2 more strongly than the core-type projection, while in layers 3, 4, and 6, the roles were reversed. Neurons in layer 5 were innervated on average equally strongly by both projections, although layer 5a preferred the matrix-type and layer 5b the core-type projection.

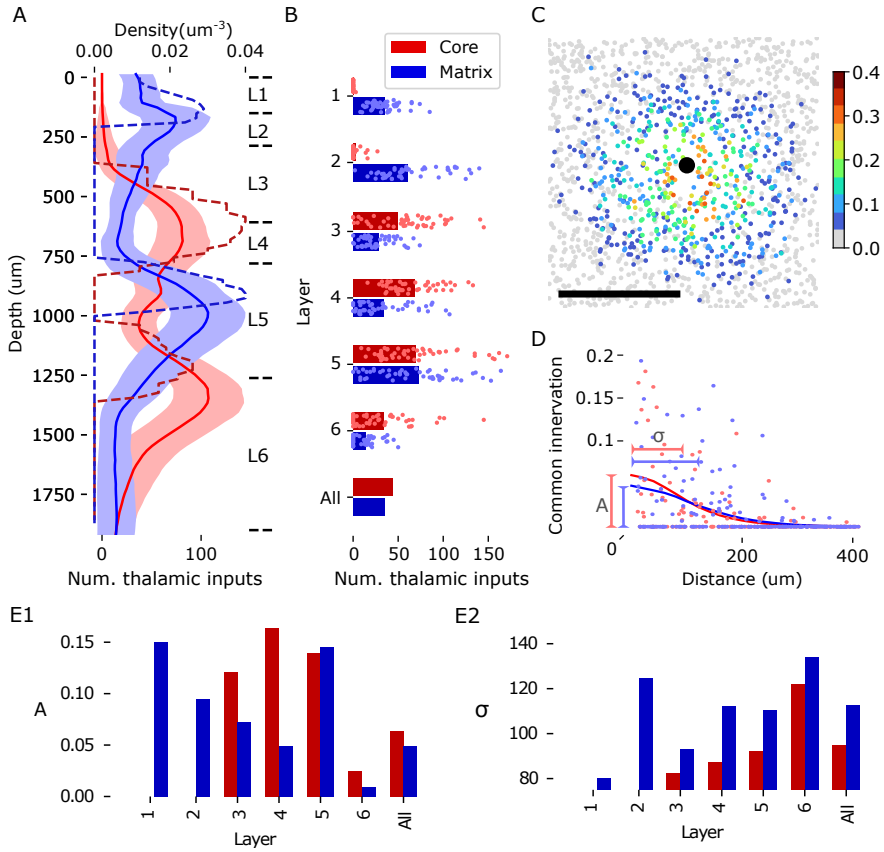

Figure 6: Anatomy of thalamic innervation. A: Depth profiles of synapse densities (dashed lines) and mean number of thalamic inputs per neuron (solid lines) for core- (red) and matrix-type (blue) thalamo-cortical projections. Shaded area indicates the standard error of mean. B: Mean number of thalamic inputs for neurons in individual layers or all neurons. Dots indicate values for 50 randomly picked neurons of the indicated layers. Colors as in A. C: Common thalamic innervation (CTI) of an exemplary neuron (black dot) and neurons surrounding it, calculated as the intersection over union of the sets of thalamic fibers innervating each of them. Scale bar: 200 μm. D: CTI of pairs of neurons at various horizontal distances. Dots indicate values for 125 randomly picked pairs; lines indicate a sliding average with a window size of 40 μm. We perform a Gaussian fit to the data, extracting the amplitude at 0 μm (A) and the standard deviation (σ). E: Values of A and σ for pairs in the individual layers or all pairs. Colors as in A. F: Clusters based on CTI of 3000 randomly selected neurons in a circular region of layer 4 by the matrix-type projection. Scale bar: 200 μm. G: Silhouette score of clusters in individual layers, evaluated against the matrix of spatial distances of the neurons.

To characterize the horizontal structure, we introduced the common thalamic innervation (CTI, see STAR*Methods) as a measure of the overlap in the thalamic inputs of pairs of neurons. As pairs with many common inputs are likely to have similar stimulus preferences, the magnitude and range of this effect has consequences for the emergence of functional assemblies of neurons. As expected from the horizontal extent of individual fibers, the CTI was distance-dependent (Figure 6C, D), and showed strong variability. Even directly neighboring pairs might not share a single thalamic afferent, leading to a sparse spatial distribution of pairs with strong overlap. A Gaussian fit of the distance dependence of CTI revealed roughly equally strong overlapping innervation for both core- and matrix-type projections (Figure 6E1). The strength of the overlap increased for lower layers in the case of core-type and decreased for matrix-type projections, while being equally

bioRxiv preprint doi: https://doi.org/10.1101/2022.08.11.503144; this version posted July 29, 2023. The copyright holder for this preprint (which was not certified by peer review) is the author/funder, who has granted bioRxiv a license to display the preprint in perpetuity. It is made available under aCC-BY-NC 4.0 International license.

strong in layer 5. The horizontal range of common innervation was larger for matrix-type projections in all layers (Figure 6E2). In summary, while the anatomy of thalamo-cortical projections introduces a spatial bias into the emergence of cortical maps, it is relatively weak on its own and supports different stimulus preferences even for neighboring pairs of neurons.

2.6 Local brain geometry affects connectivity

Cortex is often seen as a homogeneous structure with parallel layers, but at the larger spatial scales considered in this model, significant variability in its height and curvature can be observed. Our approach to connectivity allowed us to predict the impact of local brain geometry on connectivity (see also Ronan et al. (2011)). We partitioned the model into columnar subvolumes with radii of approximately $230\,\mu m$ (Fig. 7A) that we then analyzed separately. We do not claim that these columns have a biological meaning on their own, they only serve to discretize the model into individual data points each representing localized circuitry affected by local geometry.

We quantified the two main variable factors of geometry, measuring the height and *conicality* (a feature that measures the convexity of a column, see STAR*Methods) of each column (Fig. 7B). We found that differences in these factors lead to differences in relevant topological parameters, such as the modularity of the local network (Fig. 7C). This effect was mostly mediated by differences in the neuronal composition, both in terms of total neuron count (not shown) and relative counts for individual layers (Fig. 7D1). However, conicality also affected the density of connections in local, layer-specific subnetworks (Fig. 7D2), i.e., a measure that is normalized against neuron counts.

Going beyond the local, purely internal networks, we considered how much each column was innervated by the individual layers of the entire model. We predict a surprisingly strong impact of geometry, e.g., the ratio of inputs from layer 3 to inputs from layer 6 shifts from almost 2-1 in convex regions to 1-2 in concave regions (Fig. 7E1). On the other hand, we consider the total amount of inputs received, in each layer of a column. In layers 4, 5 and 6, neurons had a higher in-degree if they were members of tall columns (i.e. placed at locations of large cortical thickness). For layers 1, 2 and 3 the trend was weakened or nonexistent (Fig. 7E2). The notion of in-degree can be generalized to the *n-dimensional in-degree* measuring participation in specific, directed motifs of n+1 neurons (see STAR*Methods). While trends differed between individual layers, overall the dependence of generalized in-degree on geometrical measures increased with dimension (Fig. 7F1,F2 "full"). This was particularly driven by neurons in layer 6. Curiously, in that layer the sign of the r-values, with respect to conicality, inverted from dimensions 1 and 2 to dimensions above 2, indicating the overall innervation of layer 6 is stronger in convex regions, but the participation in higher-order motifs is stronger in concave regions.

2.7 The complexity of local and long-range connectivity requires neuronal morphologies

So far, we have analyzed single (thalamo-cortical) pathways making up less than 5% of the synapses in the model, and connectivity at scales that are already readily achievable in electron-microscopic reconstructions. The large size of the model also allowed us to characterize predicted connectivity at cellular resolution, but scales that are experimentally only accessible with regional or voxelized resolution (Oh et al., 2014; Bota et al., 2015; Scannell et al., 1995; Scholtens et al., 2014), thereby bridging the scales as outlined in the introduction. Note that the topological methods in the following sections represent and analyze the connectome as a graph, with neurons as nodes and connections between neurons as directed edges, irrespective of the number of synapses in the connection.

We began by analyzing the global structure of neuron-to-neuron connectivity in the entire model, considering local and long-range connectivity separately. The topology of synaptic connectivity at single neuron resolution has previously been described in terms of the over-expression of directed simplices (Reimann et al., 2017b). A *directed simplex of dimension* n (or n-simplex, plural n-simplices) is a neuron motif of $n+1$ neurons that are connected in a purely feed-forward

bioRxiv preprint doi: https://doi.org/10.1101/2022.08.11.503144; this version posted July 29, 2023. The copyright holder for this preprint (which was not certified by peer review) is the author/funder, who has granted bioRxiv a license to display the preprint in perpetuity. It is made available under aCC-BY-NC 4.0 International license.

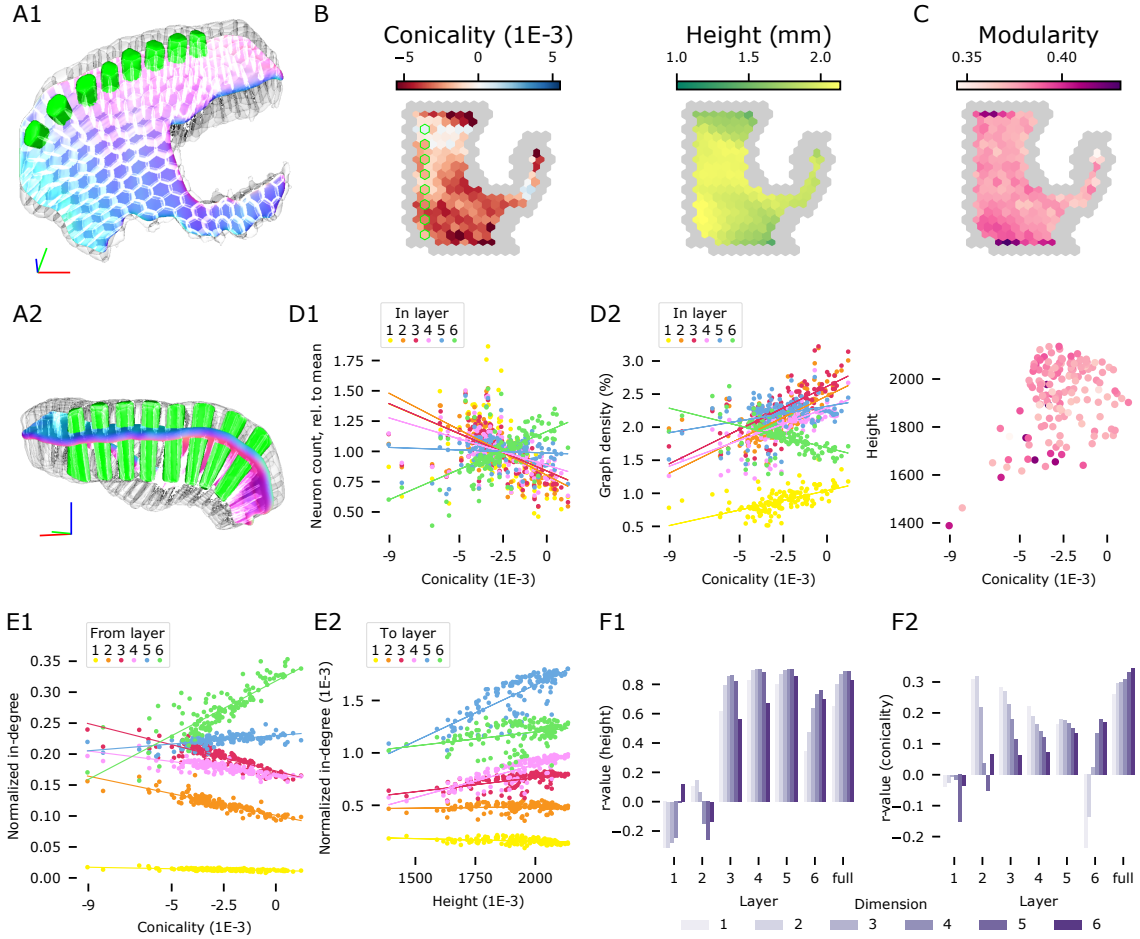

Figure 7: A1, A2: Parcellation of the modeled volume into 230 μm radius columns. Exemplary slice of columns highlighted in green. B: Geometrical metrics of column subvolumes in the flat view. Peripheral columns masked out (grey); green outline: highlighted columns in A. Left: Conicality, defined as the slope of a linear fit of depth against column radius. Negative values indicate narrowing towards L6. Right: Column height, i.e. cortical thickness at the location of the column. C: Modularity of the networks of connections within each column. Top: Overview of column positions; bottom: Against column conicality and height. D1: Conicality of columns against their laminar neuronal composition, normalized against the overall composition of the model. Colored lines indicate linear fits. D2: Conicality against the density of connections in subnetworks given by the intersections of columns with individual layers. E: Counts of afferents formed onto neurons in individual columns from neurons in the entire model. E1: Normalized in-degrees originating from neurons in individual layers, plotted against conicality. E2: In-degree of neurons in individual layers normalized by the overall in-degree in the model into each layer plotted against column height. F: r-values of linear fits against generalized, n-dimensional in-degree as in E2. F1: Of generalized in-degree against height; F2: Of generalized in-degree against conicality.

fashion, with a single *source* neuron sending connections to all others, a single *sink* neuron receiving connections from all others, and the connections between non-sink neurons forming an $n-1$-simplex (Figure 8A1, inset; Figure S11A). In particular, 0-simplices correspond to single nodes, and 1-simplices to directed edges. Simplex counts of different dimensions in a network provide a metric of network complexity and can be used to discern their underlying structure (Kahle, 2009; Curto et al., 2013; Giusti et al., 2015). Regarding function, high-dimensional simplices have been demonstrated to shape the structure of spiking correlation between neurons and membership in functional cell assemblies (Reimann et al., 2017b; Ecker et al., 2023).

In line with previous results (Reimann et al., 2017b), we found simplices up to dimension seven in the local connectivity (Figure 8A1, green). The maximal dimension did not increase compared

bioRxiv preprint doi: https://doi.org/10.1101/2022.08.11.503144; this version posted July 29, 2023. The copyright holder for this preprint (which was not certified by peer review) is the author/funder, who has granted bioRxiv a license to display the preprint in perpetuity. It is made available under aCC-BY-NC 4.0 International license.

to Markram et al. (2015) even with the larger scale of the present model, in accordance with using the same algorithm for local connectivity. However, the addition of long-range connectivity did produce a major change. In long-range connectivity alone, simplices of dimension up to 15 were observed (Figure 8A2, orange). This holds true even though local and long-range connectivity have roughly the same number of edges (2.1 billion local, 2.5 billion long-range), indicating that the higher simplex counts are not simply due to a larger number of connections. The simplex counts in the combined network of local and long-range connections are not simply the sum of the local and long-range simplex counts (Figure 8A2). They are consistently higher and also attain a higher dimensionality generating motifs of up to dimension 18, indicating a strong structural link between the two systems.

We compared the simplex counts of the model to a range of relevant controls that capture simple anatomical properties, such as the density of connections or cortical layers, but ignore the impact of neuronal morphologies (Figure 8A1,A2). This allowed us to assess the degree to which the neuronal geometry generates the complexity of the network. The control models and the parameters on which they capture were the following: the *Erdős–Rényi (ER)* model used the overall connection density, the *stochastic block model (SBM)* used density in m-type-specific pathways, the *configuration model (CM)* used sequences of in- and out-degrees, and finally the *distance block model (DBM)* used distance-dependence and neuron locations for individual m-type-specific pathways. See STAR*Methods for details.

We found that the structure of connectivity is not only determined by the parameters captured by the controls. The CM control was the closest control for long-range connectivity, suggesting that the effect of degree is important, as expected from the very long-tailed degree distributions of the long-range connectome (Figure S11A). Nonetheless, this control model still largely underestimates the complexity of the long-range network. At the same time, the DBM control was the closest control for local connectivity, showing that much of its structure is indeed determined by spatial distance under certain morphological constraints.

2.8 Simplicial cores define central subnetworks, tied together by long-range connections

Next, we investigated in which layers the neurons forming these high-dimensional structures resided by measuring *node participation*, *i.e.* the number of simplices to which a node belongs, and a measure of the node's centrality (Sizemore et al., 2018; see STAR*Methods for details). We found that in local connectivity, most simplices of dimensions 2, 3, and 4 have their source in layer 3 and their sink in layer 5. Yet, for dimensions 5 and above, we found a shift towards layer 6, with both sources and sinks found mostly in that layer. In long-range connectivity the structures are much more concentrated on layer 5, which contains both source and sink. Only for simplices of dimension greater than 8 does layer 4 provide more sources. Taken together, this indicates a robust local flow of information from superficial to deeper layers and within deep layers, with layer 5 forming a backbone of structurally strong long-range connectivity. Neurons in layer 6 form numerous simplices among themselves with no apparent output outside of layer 6, but they are known to be the source of many cortico-thalamic connections (Shepherd and Yamawaki, 2021) that are not a part of this model.

The model made an explicit distinction between m-types forming outgoing long-range connections (i.e., projecting m-types) and those that do not (Figure S11C, "proper sinks") leading to bimodal distributions of out-and total degrees in the corresponding DBM and SBM controls (Figure S11A). In contrast, the actual long-range network has a unimodal, long-tailed degree distribution, similar to biological neuronal networks (Giacopelli et al., 2021). This further demonstrates that the m-types alone can not capture the specific targeting between neuron groups without their actual morphologies.

One type of connectivity specificity that has been found in biological neuronal networks (Towlson et al., 2013) is the formation of a rich club (Zhou and Mondragon, 2004; van den Heuvel and Sporns, 2011). This is characterized by a rich-club curve, which measures whether high degree

bioRxiv preprint doi: https://doi.org/10.1101/2022.08.11.503144; this version posted July 29, 2023. The copyright holder for this preprint (which was not certified by peer review) is the author/funder, who has granted bioRxiv a license to display the preprint in perpetuity. It is made available under aCC-BY-NC 4.0 International license.

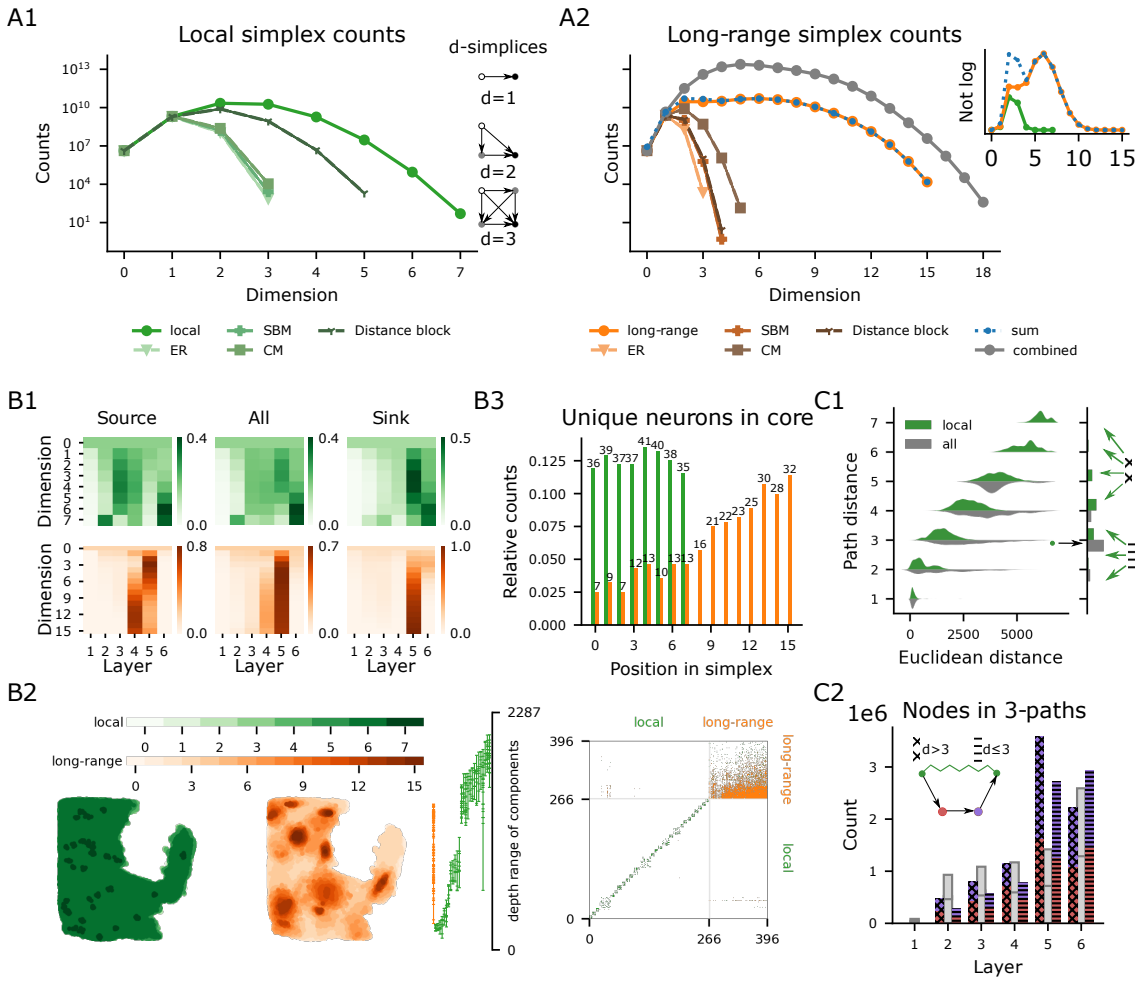

Figure 8: Global connectivity structure local vs. long-range. A1: Simplex counts of the local connectivity network and several types of random controls (see text). Examples of d-simplices for $d = 1$, 2, and 3. Intuitively, an n-simplex is formed by taking an $n-1$-simplex and adding a new node to which all neurons connect (sink). A2: In orange shades, simplex counts of the long-range connectivity network and several types of random controls. In gray, simplex counts of the combined network and in blue the sum of the local and the long-range simplex counts. Inset: local, long-range and the sum of simplex counts on a linear scale. B1: Normalized node participation per layer. Top/bottom row: Local/long-range connectivity network. Left to right: Participation as source, in any position, and as a sink of a simplex. B2: From left to right: Spatial location of the cells in the simplicial n-cores in flat coordinates for all n. Depth coordinates for each connected component in the simplicial cores (cells participating in simplices of maximal dimension) each dot marks the depth of a neuron in that component. Adjacency matrix of the simplicial cores with respect to local (green dots) and long-range (orange dots) connections. B3: Number of unique cells in the simplicial cores present in each position of a simplex. C1: Right: Distribution of path distances between pairs of neurons in the local simplicial core; green: along only local edges; grey: along all edges. Left: Euclidean distances between pairs at a given path distance. Arrows: See C2. C2: Total Number of neurons in all paths of length 3 between neurons of the local core which are at distance 3 in the combined circuit (black arrow in C1) split by location. Red/purple: at positions 2 and 3 respectively; grey: expected from randomly assigned m-types while maintaining the global distribution. Cross-/stripe-patterned: For pairs at path distances greater/less-or-equal than 3 along local edges only (green arrows in C1).

bioRxiv preprint doi: https://doi.org/10.1101/2022.08.11.503144; this version posted July 29, 2023. The copyright holder for this preprint (which was not certified by peer review) is the author/funder, who has granted bioRxiv a license to display the preprint in perpetuity. It is made available under aCC-BY-NC 4.0 International license.

nodes are more likely to connect together, compared to the CM control (see STAR*Methods). We observe that the local network has a rich-club effect, but it is not stronger than expected in a spatially finite model with distance-dependent connectivity (Figure S12B1/2). On the other hand, the long-range network does not exhibit a rich-club effect, see Figure S12B2 bottom, showing that high degree nodes are not central to the network.

When we generalized the rich club analysis to higher dimensions by considering node participation instead of degree (Opsahl et al. (2008); see STAR*Methods for details) a different picture emerged (see Figure S12B3). We found that the rich club coefficients in the long-range network increased with dimension, while the opposite happens for the local network. We speculate that this effect persists after normalization with respect to relevant controls. Unfortunately, this cannot be currently verified since generating appropriate random controls for these curves is an open problem currently investigated in the field of random topology (Unger and Krebs, 2022). Nonetheless, this indicates that central nodes strongly connect to each other forming a structural backbone of the network that is not determined by degree alone.

We studied these structural backbones, by focusing on the *simplicial cores* of the networks, which is a higher dimensional generalization of the notion of network core, which is determined by degree alone (see STAR*Methods). The general trend observed is that the local network is distributed, while the long-range network is highly localized. First in terms of the locations of neurons participating in the cores (Figure 8B2 left; green vs. orange), and their laminar locations (Figure 8B2 right). Second, even though the numbers of neurons in the local and long-range cores are in the same order of magnitude, the local core has 26 disconnected component while the long-range core is fully connected (Figure 8B3 bottom). Finally, the long-range core was successively more strongly localized towards the source position, where only seven unique neurons were the sources of all of the $15,108$ highest-dimensional long-range simplices (Figure 8B3 top).

Finally, we studied the interactions between the local and long-range networks, specifically, the ability of long-range connnectivity to form short-cuts between neurons of the local core. Even though the sub-network on the nodes in the local core has multiple connected components (Figure 8B2), when paths through nodes outside the core are allowed, it is fully connected. When only local connectivity was considered, the path distances between core neurons were widely distributed between one and seven with a median of four and a strong dependence on their euclidean distance (Figure 8C1, green). On the other hand, when long-range connections were added the maximum path distance drops to five, with a negligible number of pairs at that path distance. The median path distance drops to three, and the dependence of the path distance on the euclidean distance of the pairs nearly disappears (Figure 8C1, grey). Crucially, even though the number of edges almost doubled with the addition of long-range connections, the number of direct connections remained negligible; instead paths of length three seem to be dominant for information exchange between neurons.

We therefore studied these paths of length three in the combined circuit in more detail, labeling the neurons along them from position 1 (start-node) to position 4 (end-node). We found that layer 5 (the layer with the highest outgoing edge probability, see Figure S11B) is over-represented in nodes in positions 2 and 3 compared to a random assignment of m-types (Figure 8C2). Moreover, the over-representation depends on the path distance between the start-node and end-node within the local network: when the value is larger than three (bars hatched by crosses), the effect is stronger than for pairs at a distance three or less (bars hatched by horizontal bars). This demonstrates and quantifies how neurons in layer 5 act as "highway hubs" providing shortcuts between neurons that are far away from each other in the local circuit.

bioRxiv preprint doi: https://doi.org/10.1101/2022.08.11.503144; this version posted July 29, 2023. The copyright holder for this preprint (which was not certified by peer review) is the author/funder, who has granted bioRxiv a license to display the preprint in perpetuity. It is made available under aCC-BY-NC 4.0 International license.

3 Discussion

We have presented a model of the non-barrel primary somatosensory cortex of the juvenile rat that represents its neuronal and - particularly - synaptic anatomy in high detail.

The model comprises a spatial scale that allows for the study of cortical circuits not only as isolated functional units, but also their interactions along inter-regional connections. It also demonstrates how novel insights that are not readily apparent in disparate data and individual models can be gained when they are combined in a way that creates a coherent whole. Specifically, we were able to make multiple predictions about the structure of cortical connectivity that required integration of all anatomical aspects potentially affecting connectivity. While connectivity is affected by aspects not apparent in neuronal anatomy (see below), proximity of an axon to the postsynaptic process is a requirement for the formation of a synapse, providing a strong constraint.

At the scale of this model, anatomical aspects affecting connectivity went beyond individual neuronal morphologies and their placement, and included intrinsic cortical curvature and other anatomical variability. This was taken into account during the modeling of the anatomical composition, e.g. by using three-dimensional, layer-specific neuron density profiles that match biological measurements, and by ensuring the biologically correct orientation of model neurons with respect to the orientation towards the cortical surface. As local connectivity was derived from axo-dendritic appositions in the anatomical model, it was strongly affected by these aspects. However, this approach alone was insufficient at the large spatial scale of the model, as it was limited to connections at distances below $1000\mu m$. While we found that it generated the right amount of connectivity within a somatosensory subregion, we combined it with a second algorithm for inter-regional connectivity. The algorithm is parameterized by a combination of overall pathway strength, topographical mapping and layer profiles, which together describe a probability distribution for the segments of long-range axons, i.e. an average axonal morphology, using established concepts. On the dendritic side, the algorithm takes individual neuronal morphologies and their placement into account.

Recreating electron-microscopic analyses of connectivity *in silico*, we could then predict limitations of predicting connectivity from anatomy and characterize the additional mechanisms shaping connectivity. Conceptually, a number of mechanisms determine the structure of synaptic connectivity, which we will list from general and large-scale to specific and micro-scale: First, large-scale anatomical trends over hundreds of μm, given by non-homogeneous (e.g. layered) soma placement and broad morphological trends (e.g. ascending axons). These are trends that can be captured by simple distance or offset-dependent connectivity models (Gal et al., 2020). Second, small-scale morphological trends captured by axonal and dendritic morphometrics such as branching angles and tortuosity. These are trends that require the consideration of individual morphologies and their variability instead of average ones. Third, the principle of cooperative synapse formation (Fares and Stepanyants, 2009) formalizing an avoidance of structurally weak connections. Fourth, any type-specific trends not captured by neuronal morphologies, such as local molecular mechanisms and type-specific synaptic pruning. Fifth, non-type specific synaptic rewiring e.g. through structural plasticity. We will refer to these aspects as (L)arge-scale, (S)mall-scale, (C)ooperativity, (T)ype-specificity and (P)lasticity respectively, and we argue that for the explanation of the connectome, the more general explanations should be exhausted first, before moving on to more specific ones. Also note that this classification is not considering the underlying developmental *causes*, but instead associates anatomical and non-anatomical predictors with the structure of the connectome. Based on the results presented here and previous results, we can predict their relevance in determining the connectome of different neuron types (Table 2).

(L) has been shown to accurately predict large-scale connectivity trends, giving rise to *Peters' rule* (Peters and Feldman, 1976; Garey, 1999, although the exact meaning of Peters' rule is debated, see Rees et al., 2017). In Gal et al., 2017; Reimann et al., 2017a; Gal et al., 2020, it has been demonstrated that (L) alone does not suffice to explain non-random higher order trends in excitatory connectivity, while the combination of (L,S,C) does, explicitly highlighting the importance of (S). More specifically, Reimann et al. (2017b) found that (L,C) explains overexpression

bioRxiv preprint doi: https://doi.org/10.1101/2022.08.11.503144; this version posted July 29, 2023. The copyright holder for this preprint (which was not certified by peer review) is the author/funder, who has granted bioRxiv a license to display the preprint in perpetuity. It is made available under aCC-BY-NC 4.0 International license.

of reciprocal connectivity in cortical circuits, but (L,S,C) is required to match the biological trend for clustered connectivity. Our comparison to the results of Motta et al. (2019) cannot capture the role of (L), as the scale of the considered volume is too small. But it demonstrates that some non-random targeting trends can be explained by (S,C) and highlights the importance of (C). Further, the overall lower specificity of excitatory axon fragments indicates that (T) may not play a role for them. Similarly, the comparison to Schneider-Mizell et al. (2023) shows that (T) is not required to explain the connectivity of "distal-targeting" (i.e., Sst+) neuron types. Conversely, for "perisomatic-targeting" types (PV+ basket cells) (T) was required to match the distribution of postsynaptic compartment types. Although, it should be noted that the number of unique morphological reconstructions in the model is lower for inhibitory than excitatory neurons, thus potentially underestimating the impact of (S). Additionally, the number of potential synapses remaining after applying an optimized (T)-type mechanism was too large to be sustained by the axons, implying a crucial role of (P) in reducing it further. This is in contrast to "inhibitory-targeting" neurons, where an optimized (T)-type pruning lowered the synapse count so much that no space for (P) remained. For the "sparsely-targeting" neurons of Schneider-Mizell et al., 2023 we developed two competing hypotheses, one predicting no role for (T) and 70% of their synapses volumetrically transmitting, i.e. without clear postsynaptic partner, and the other predicting a role for (T) similar to the perisomatic-targeting neurons. It is notable, that our models of the effects of (T) in this work were based purely on avoidance of types of postsnaptic compartments while pruning the set of potential synapses. This is in contrast to (Romani et al., 2023) who had to increase the maximum distance between axon and dendrite that is considered a potential synapse to model of the strong specificity of excitatory to inhibitory pathways in local hippocampal connectivity. Conceptually, this is based on attraction rather than avoidance and weakens the impact of (C) in favor of (T). This could also be used to further increase the specificity of VIP+ neurons for inhibitory partners in the model.

Table 2: Anatomical, morphological and other aspects affecting connectivity and our predictions for their relevance for efferents of different neuron types. See main text for an explanation of the individual aspects.

Axon type	(L)arge-scale morphological	(S)mall-scale morphological	(C)ooperativity	(T)ype-specificity	(P)lasticity
Cortex, EXC.	+	++	++	-	+
Cortex, BCs	+	+	+	+	+
Cortex, Sst+	++	+	+	-	+
Cortex, VIP+	+	-	+	++	-
Cortex, NGC and L1	++	+	-	+ / -	+
Hippocampus, EXC.	+	-	+	++	+

Second, we were able to predict the effect of cortical anatomical variability on neuronal composition by increasing or decreasing the space available for individual layers. If we assume that each layer has a given computational purpose (Felleman and Van Essen, 1991), then this may have functional consequences. It is possible that cortical circuits compensate for this effect, either anatomically (e.g. using different axon or dendrite morphologies), or non-anatomically. Either case would imply the existence of an active mechanism with the possibility of malfunction. Alternatively, function of cortical circuits is robust against the differences in wiring we characterized. This can be studied either *in vivo*, or *in silico* based on this model.

Third, we predicted constraints on the emergence of cortical maps from the anatomy of thalamo-cortical innervation, i.e., from the combination of: shape and placement of cortical dendrites, the specific layer pattern formed by thalamo-cortical axons, and their horizontal reach. We demonstrated how differences in these parameters may affect the distances between neuron pairs with similar stimulus preferences. At the lower end, very different preferences are supported even between neighboring neurons. At the higher end, neurons further than $\approx 350\mu m$ apart are likely

bioRxiv preprint doi: https://doi.org/10.1101/2022.08.11.503144; this version posted July 29, 2023. The copyright holder for this preprint (which was not certified by peer review) is the author/funder, who has granted bioRxiv a license to display the preprint in perpetuity. It is made available under aCC-BY-NC 4.0 International license.

to sample from non-overlapping sets of thalamic inputs. Other mechanisms will ultimately affect this - chief among them structural synaptic plasticity - this can be thought of as the ground state that plasticity is operating on.

Fourth, we predicted the topology of synaptic connectivity with neuronal resolution at an unprecedented scale, i.e. combining local and long-range connectivity. We found that the structure of neither can be explained by connection probabilities, degree-distributions, or distance-dependence alone, not even when individual pathways formed between morphological types are taken into account. We expect the long-range network to have a small-world topology, but computing small-world coefficients for a network of this size is infeasible (see STAR*Methods).

Fifth, we predict that the long-distance connectivity forms a strong structural backbone distributing information between a small number of highly connected clusters. The paths within the long-range network strongly rely on neurons in layer 5 and form short-cut paths for neurons further away than around $2mm$; for smaller distances, local connectivity provides equivalent or shorter paths.

All these insights required the construction of an anatomically detailed model in a three-dimensional brain atlas; additionally, most of them required the large spatial scale we used. Their functional and computational implications are difficult to predict without also considering data on neuron activity. To that end, an accompanying manuscript describes our modeling of the physiology of neurons and synapses, along with a number of *in silico* simulation campaigns and their results.

This iteration of the model is incomplete in several ways. Most of them stem from compromises and generalizations that were made to be able to parameterize the process with biological data. Further, we made a number of assumptions about the biological systems that we explicitly list in Supplementary Section 5.2. While violations of any of these assumptions affect the validity of the model, this is a natural step during modeling. The largest uncertainty results from the topographical mapping of long-range connectivity that was fit against biological data for each pair of regions, then adapted from mouse to rat. We expect our results related to long-range connectivity to hold as long as axons have a limited horizontal extent with spatial targeting described by a topographical mapping, independent of the specific structure of the mapping. Additionally, we demonstrated that while inhibitory connectivity can be predicted from axo-dendritic appositions, the type of post-synaptic compartment should be taken into account when reducing the set of potential synapses. However, detailed modeling at this scale is a highly complex process that requires constant iteration, as a model can never be proven to be right, only to be wrong. Therefore, scientific uses of the model will always have to be conducted in parallel with refinement of known weaknesses. Thus, we decided to publicly release the model as described in this work as an invitation to the community to participate in such refinement.

bioRxiv preprint doi: https://doi.org/10.1101/2022.08.11.503144; this version posted July 29, 2023. The copyright holder for this preprint (which was not certified by peer review) is the author/funder, who has granted bioRxiv a license to display the preprint in perpetuity. It is made available under aCC-BY-NC 4.0 International license.

4 STAR*Methods

Key resources table

REAGENT or RESOURCE	SOURCE	IDENTIFIER
Deposited data		
Neuron morphology reconstructions	Markram et al.	10.5281/zenodo.8155899
In-vivo morphology reconstructions	This paper	10.5281/zenodo.8155899
Cell density layer profiles	Keller et al., 2019	From original publication 10.3389/fnana.2019.00078
Voxelized brain atlas	This paper	10.5281/zenodo.8155899
Cell density atlas	This paper	10.5281/zenodo.8155899
Orientation and flat coordinate atlas	Bolaños-Puchet and Reimann, prep	10.5281/zenodo.8165005
Thalamo-cortical synapse densities	Meyer et al., 2010	Digitized figures
Thalamo-cortical axon widths	Janelia MouseLight Economo et al., 2016	Reported in text
Mean axonal bouton densities	Reimann et al., 2015	From original publication 10.3389/fncom.2015.00120
Mean number of synapses per connection	Reimann et al., 2015	From original publication 10.3389/fncom.2015.00120
Resulting anatomical model	This paper	10.5281/zenodo.8155899
Software and algorithms		
Model loading and interaction	This paper	10.5281/zenodo.8026852
Model and analysis	This paper	10.5281/zenodo.8016989
Topological analysis of connectivity	This paper	Zenodo DOI

Resource availability

Lead contact

Further information and requests for data and code should be directed to and will be fulfilled by the lead contact: Michael W. Reimann (michael.reimann@epfl.ch)

Materials availability

No materials were used in this computational work

Data and code availability

- Data on cell densities, bouton densities and mean numbers of synapses per connection were reported in original publications. Their DOI are listed in the Key Resources Table.
- Data on synapse densities of thalamo-cortical inputs and their projection axon widths are reported in figures and text in this publication.
- Volumetric atlasses, neuron reconstructions, the parameterization of long-range connectivity in JSON format, and the description of the model in SONATA format (Dai et al., 2020) have been deposited at Zenodo and are publicly available as of the data of the publication. The DOIs are listed in the key resources table.
- Original code has been deposited at Zenodo and is publicly available as of the date of publication. DOIs are listed in the key resources table.
- Any additional information required to reanalyze the data reported in this paper is available from the lead contact upon request.

bioRxiv preprint doi: https://doi.org/10.1101/2022.08.11.503144; this version posted July 29, 2023. The copyright holder for this preprint (which was not certified by peer review) is the author/funder, who has granted bioRxiv a license to display the preprint in perpetuity. It is made available under aCC-BY-NC 4.0 International license.

4.1 Method details

4.1.1 Preparation of voxelized atlasses

First and foremost, the departure from a simplified hexagonal geometry (as in the NMC model Markram et al. (2015)), required a digital brain atlas defining the anatomy of the region. To that end, we took as starting point the Paxinos and Watson (2007) adult rat brain atlas, processed individual digitized slices, aligned them and labeled them to assemble a smooth three-dimensional volume with region annotations. The resulting atlas was then scaled down from the dimensions of adult rat to juvenile (P14) rat brain by reducing the size of individual voxels from $40\mu m$ to $38.7348\mu m$. The scaling factor was based on the ratio of S1HL thicknesses at those ages ($2082\mu m$ for juvenile vs. $2150\mu m$ for adult). Finally, supplementary atlas datasets were generated as described in Bolaños-Puchet and Reimann (prep). These datasets provide additional spatial information required to ensure biologically accurate placement and orientation of dendritic trees (see below). First, the normalized cortical depth (between 0 and 1) at each point; second, the local orientation as a vector pointing towards the cortical surface at each point; third, the total cortical thickness at each point, i.e., the length of the shortest path from the cortical surface to the bottom of layer 6 passing through that point.

Additionally, we followed Bolaños-Puchet and Reimann (prep) to produce a *flat map* of somatosensory regions, that is, a coordinate transformation associating each voxel with a two-dimensional projection into the plane. This can be used to create a flat view of region annotations that is crucial for the description of the topographical mapping of long-range synaptic connectivity (see below). In short, to produce the flat map, a projection surface was defined by reconstructing a mesh from all points at a relative cortical depth of 0.5. Next, the local orientation field in the supplementary atlas was numerically integrated, yielding streamlines that were used to project each voxel center onto the projection surface. Finally, the projection surface was flattened with an authalic (area-preserving) algorithm. The main property of the resulting flat map is that in any flat view derived from it, each pixel represents a subvolume of cortex that spans all layers, akin to a cortical column.

4.1.2 Reconstruction of neuron morphologies

Neuronal reconstructions were collected with two techniques: neurons were either filled with biocytin in a brain slice and reconstructed (Markram et al., 2015), or were filled with a fluorescent dye *in vivo* and reconstructed (Buzás et al. (1998); Karube and Kisvárday (2011)). In total 1017 unique reconstructions were used, 896 of which were previously used in Markram et al. (2015), 63 were new *in vitro* reconstructions, and 58 were new *in vivo* reconstructions.

Animal surgery Normal C57BL/6 mice (P52-60) were used which were bred and maintained in the animal house facility of Department of Anatomy, Physiology and Embryology under appropriately controlled conditions (approval of Local Ethics Committee for Animal Research Studies at the University of Debrecen in line with European Union guidelines for the care of laboratory animals, Directive 2010/63/EU).

For initial anesthesia, animals were injected with pentobarbital (0.15ml (6mg/ml), i.p.). Prolonged anesthesia was achieved by injecting 0.05 ml every 60-90 minutes depending on the reaction to the toe-test. Head restraining was used and craniotomy performed in both hemispheres at coordinates ML 1.5 - 2 mm ; AP 0.5 - 1 mm (Paxinos and Watson, 2007) in order to expose the primary somatosensory cortex at the representation of the (hind-limb and fore-limb). We applied the topical anesthetic Lidocaine (Xylocaine gel, Egis Gyógyszergyár ZRT, Hungary) to all surgical wounds and pressure points. A custom-made plastic chamber (prepared by cutting a ring from a 1 ml plastic syringe) was mounted on the skull using super glue and was surrounded by 4% agar (VWR International Kft, Hungary). Then, the cortex was exposed by making a slit on the dura mater with the bent tip of a 14 gauge hypodermic needle.

bioRxiv preprint doi: https://doi.org/10.1101/2022.08.11.503144; this version posted July 29, 2023. The copyright holder for this preprint (which was not certified by peer review) is the author/funder, who has granted bioRxiv a license to display the preprint in perpetuity. It is made available under aCC-BY-NC 4.0 International license.

Single neuron labelling For this purpose, borosilicate glass pipettes (GB150F-8P, Science Products GmbH, Germany) were pulled (Model P-97, Sutter Instrument Co., USA) with a resistance in the range of 60-80MΩ (bevelled on a BV-10M beveler, Sutter Instrument Co., USA) and filled with 1M KCl containing 2% biocytin (Sigma-Aldrich Chemie GmbH, Germany). The microelectrode was attached to a hydraulic microdrive (MHW-4 Narishige, Japan) and the tip guided in the cortex under the guidance of a surgical microscope (OP-MI, Zeiss). Then the chamber was then filled with 4% agar (VWR International Kft, Hungary) for better stability of the micropipette. Neuronal activity was recorded and amplified with AxoClamp-2A (Axon Instruments Inc., USA). After filtering, the signal was displayed on an oscilloscope and an audio monitor to aid and control intracellular penetration. Successful penetration of the cell membrane was indicated by a sudden drop of the resting membrane potential (below -40mV) while applying 0.05 nA in the step-current mode (put here stimulus configuration from Master-8). Then, biocytin was injected with +2 nA using a duty cycle of 400 msec on and 200 msec off typically for 20 min. In each hemisphere 1-3 penetrations were made with approximately 0.3 mm spacing from each other. Neuronal activity was searched blindly across the entire cortical depth.

Histology The animals received a lethal dose of anesthetics and were perfused transcardially first with the washing medium (oxygenated Tyrode's solution) for 2 min or until the blood showed clearing and then with a fixative (approx. 100 ml) containing 2% paraformaldehyde (VWR International Kft, Hungary) and 1% glutaraldehyde (Sigma-Aldrich Chemie Gmbh, Germany) in 0.1 M phosphate buffer (PB, pH 7.4) for 50 minutes. Next, the brain was removed from the skull and tissue blocks containing the region of interest were dissected. A series of 60-80 um thick vibratome (Leica VT1000S, Leica Biosystem) sections were cut in the coronal plane and collected in 5x10 lots in glass vials. The sections were washed in 0.05M Tris-buffer saline (TBS, 10 min) and 0.05M TBS containing 0.1% Triton X-100 (2 x 10 min) and incubated at 4°C in avidin-biotin complexed-HRP (ABC-Elite kit, Vector Laboratories, Inc., USA), diluted 1:200 in 0.05M TBS containing 0.1% Triton X-100 (Sigma-Aldrich Chemie Gmbh, Germany) for overnight. Then the sections were washed in TBS for 2 x 10 min and in TB for 10 min. They were treated with 0.05% DAB (3.3' diaminobenzidine-4HCl, Sigma-Aldrich Chemie Gmbh, Germany) diluted in 0.05 M TB containing 0.0025% CoCl2 for 30 min while agitating on an electric shaker. Finally the labelling was visualized in the presence of 0.1% H2O2 (5 min to 10 mins). After washing the sections in 0.05M TBS (3 x 10 min) and 10 min in 0.1 M PB the quality of the DAB reaction and the presence of intracellularly labelled cells were inspected while wet under a light microscope (x10 objective). All sections of blocks containing strongly labelled neurons underwent osmification, dehydration and resin embedding in order to retain the 3D structure of their axons and dendrites. Accordingly, sections were treated with 1% OsO4 (osmium tetroxide, PI Chem Supplies, USA) diluted in 0.1% PB for 15 minutes. After rinsing in 0.1M PB for 3x10 min, they were dehydrated in ascending series of ethanol (50, 70, 90, 95 per cent and abs ethanol), propylene oxide, each step for 2x10 min, and submerged in resin (Durcupan, Sigma-Aldrich Chemie GmbH, Germany) overnight at room temperature. Finally, the sections were mounted on glass slides, coversliped and cured at 56oC for 24 hours (Somogyi and Freund, 1989).

Morphological neuron reconstruction Labelled neurons were reconstructed in 3D using the Neurolucida neuron reconstruction system running on Windows XP platform (Neurolucida v.8.23, MicroBrightField Inc., Williston, USA). For this purpose a Leica DMRB microscope (x100 objective) was coupled to a motorized XY-stage and a z-motor via a stage controller (Märzhäuser Wetzlar GmbH & Co. KG, Wetzlar, Germany). Each neuron was reconstructed from 20-32 adjoining sections. Neighboring sections were aligned using the 3-point alignment and the least-squares algorithm for the cut ends of labelled processes and fiducial landmarks such as the contour of cut blood vessels. The cell body, dendrites, axons and axon terminals were reconstructed together with their thickness value.

4.1.3 Morphology curation and classification

All morphological neuron reconstructions (see Section 4.1.2) were curated and repaired to correct reconstruction errors and slicing artifacts, as described in Markram et al. (2015). They were

bioRxiv preprint doi: https://doi.org/10.1101/2022.08.11.503144; this version posted July 29, 2023. The copyright holder for this preprint (which was not certified by peer review) is the author/funder, who has granted bioRxiv a license to display the preprint in perpetuity. It is made available under aCC-BY-NC 4.0 International license.

then classified based on the following strategy. Both interneurons and pyramidal cells were first classified by expert reconstructors according to their observed shapes by inspection through the microscope. The expert classification of pyramidal cells, which is based on the shape of the apical dendrites, was then used as input for the training of the algorithms for the objective classification as presented in Kanari et al. (2019). The objective classification was performed based on the *topological morphology descriptor* (TMD) (Kanari et al., 2018), which encodes the branching structure of neuronal trees. The TMD of apical trees was extracted from all morphological reconstructions and was used to train a decision tree classifier for the objective classification of cells into distinct groups. See Fig. S5 for exemplary excitatory morphologies and their features. Conversely, interneurons have been classified by experts based on their axonal shapes and therefore the topological morphology descriptor of dendrites could not be applied for the objective classification of interneurons.

The expert-proposed scheme comprised 60 morphological types (m-types) (18 excitatory and 42 inhibitory). The m-types of pyramidal cells are distinguished first by layer and further by shape of their tuft, such as untufted (UPC) and tufted (TPC) cells; and finally into subclasses (A:large tufted, B:late bifurcating, C:small tufted). The results of the objective classification of pyramidal cells were then used to validate this classification scheme. A classification scheme was deemed valid if the TMD was significantly different between classes. This was the case for classes in all layers except for a distinction between two subgroups in layer 3 (L3_TPC:A vs. L3_TPC:B), which was consequently discarded. Instead we performed an unsupervised clustering of all tufted pyramidal cells in layer 3 based on their TMD and found a different split into two classes, best described as large tufted (L3_TPC:A) and small tufted (L3_TPC:C), which we then used in the model. The resulting list of m-types is found in Table S1.

In the remaining layers the results of the objective classification were used to validate the class assignments of individual pyramidal cells. We found the objective classification to match the expert classification closely (i.e., for 80–90% of the morphologies). Consequently, we considered the expert classification to be sufficiently accurate to build the model. To increase the morphological variability in the model we combined axon reconstructions with soma and dendrite reconstructions from other neurons of the same m-type (*mix & match*; Markram et al. (2015)).

4.1.4 Preparation of cell density data

Inhibitory cell densities were constrained following Keller et al. (2019). In brief, several datasets were combined to provide depth profiles of densities for successively more granular neuron classes (Fig. S1). The first dataset consists of neuronal soma density estimations, using antibody stains of neuronal nuclear protein (NeuN) and γ-aminobutyric acid (GABA) from rat neocortex (n = 6, Keller et al. (2019)). Cell counts provided mean densities and a measure of inter-individual variability (Markram et al., 2015). Cell counts were obtained from a single rat in this dataset, and their positions were annotated and divided into 100 equal-width bins extending from the top of layer 1 (L1) to the bottom of layer 6 (L6) (Keller et al., 2019). This provided depth profiles of both total neuron (from NeuN) and inhibitory neuron densities (from GABA). A similar profile was also estimated from immunostaining with calbindin (CB), calretinin (CR), neuropeptide Y (NPY), parvalbumin (PV), somatostatin (SOM) and vasoactive intestinal peptide (VIP) (at least three slices from at least two rats) (Keller et al., 2019). All stains were corrected for shrinkage (Ghobril, 2015). A single-neuron reverse transcription polymerase chain reaction (RT-PCR) dataset (Toledo-Rodriguez et al., 2005) allowed mapping of biochemical markers to morphological types, by finding spatial distributions of morphological cell types that would reproduce the biochemical marker distribution (Keller et al., 2019). Whenever the classification could not be resolved down to morphological types (i.e., excitatory cells, neurogliaform cells, L1 cells, etc.), an estimation of the fractions of subtypes was used (Muralidhar et al., 2014). The depth profile of excitatory neuron densities was further subdivided into subtypes, maintaining the same layerwise proportions of these types as in previous work (Markram et al., 2015). The final output of this process was a dataset of neuron density as a function of cortical depth for each of the 60 morphological types (Table S1).

bioRxiv preprint doi: https://doi.org/10.1101/2022.08.11.503144; this version posted July 29, 2023. The copyright holder for this preprint (which was not certified by peer review) is the author/funder, who has granted bioRxiv a license to display the preprint in perpetuity. It is made available under aCC-BY-NC 4.0 International license.

4.1.5 Voxelized neuronal composition

To prepare the modeled volume for cell placement, we first associated each voxel of the atlas with a cortical layer. We assumed layer boundaries to be at the same normalized depth at each point of the region. The depths, derived from Markram et al. (2015), are listed in Table S2. As a voxel atlas of normalized depths was provided as an input, layer identities could be readily looked up from that table. Similarly, neuron densities for each voxel of the atlas were produced from the vertical density profiles that served as inputs (see Sec. 4.1.4) by looking up the corresponding values using the normalized depth.

4.1.6 Neuron placement

Neurons were placed into the volume by first generating soma positions and annotating them with a morphological type according to the voxelized densities generated. Next, for each location we selected a reconstructed morphology from the annotated morphological type. As previously (Markram et al., 2015), we tried to select an appropriate reconstruction taking also the variability within a morphological type into account. For instance, the largest exemplars of layer 5 pyramidal cells cannot be placed close to the top of the layer, as otherwise their tuft would stick out of the top of layer 1. We selected morphologies by scoring them according to how well manually identified features, such as dendritic tufts or horizontal axonal branching, would land in the biologically appropriate layers, when placed at any given location. The placement rules that were used were the same as in Markram et al. (2015) and are listed in Table S3.

Previously, this process was aided by the use of a simplified geometry where layer boundaries were formed by parallel planes. To execute the algorithm in a realistic brain volume, we used auxiliary voxel atlasses (see Sec. 4.1.1; (Bolanos-Puchet and Reimann, 2022)). The first atlas contained for each voxel the normalized depth of its center point, i.e., a value between 0 and 1 where 0 would indicate its placement at the top of layer 1 and 1 the bottom of layer 6. The second atlas contained for each voxel the total thickness of the cortex at that location. As layer boundaries in the model were always placed at fixed normalized depths (Table S2), we could calculate the absolute distance of the voxel to any layer boundary by subtracting their normalized depths and multiplying the result with the local cortical thickness. Based on this, we calculated the overlap of the dendritic and axonal features of a candidate morphology with the target layer interval (Fig. S6). Morphology selection was then performed as previously (Markram et al., 2015), that is, a morphology was selected randomly from the top 10% scorers for a given position.

4.1.7 Modeling synaptic connectivity

Local connectivity To determine the structure of synaptic connectivity between neurons, data on numbers of synapses and their locations were required. Previous data for mean bouton densities on axons of various neuron types, and number of synapses per connection (Reimann et al., 2015), were used and generalized to all nbS1 subregions. The data was then used as described in (Reimann et al., 2015). Similar to neuronal morphologies (see above), there is no evidence for anatomical differences in connectivity between nbS1 subregions, with the exception of barrel cortex (not included in the model).

Long-range connectivity Due to the larger spatial scale of the present model compared to Markram et al. (2015), additional data was required to further constrain synaptic connectivity at a global scale. To that end, we referred to data on relative strengths of synaptic connections from the Allen Mouse Brain Connectivity Atlas (Harris et al., 2019), and generalized it for use with a rat model. We began by scaling the relative connection densities of Harris et al. (2019) to absolute densities in units of synapses per μm^3. That is, the entire voxel-to-voxel connection matrix of intra-cortical connectivity was scaled to match the average total density of synapses measured in electron microscopy (Schüz and Palm, 1989).

bioRxiv preprint doi: https://doi.org/10.1101/2022.08.11.503144; this version posted July 29, 2023. The copyright holder for this preprint (which was not certified by peer review) is the author/funder, who has granted bioRxiv a license to display the preprint in perpetuity. It is made available under aCC-BY-NC 4.0 International license.

Next, we summed the densities over voxels belonging to pairs of nbS1 subregions, resulting in a 6 x 6 connection matrix of synapse densities in pathways between and within regions. We mapped this matrix to rat nbS1 by finding corresponding regions in the mouse and rat atlases (Fig. S2A). Here, we assumed that synapse densities in these pathways are comparable between mouse and rat, although the larger dimensions of the rat brain resulted in larger absolute synapse counts (Fig. S2C).

We used the same mapping to generalize the spatial structure of the targeting of connections between regions from mouse to rat. This refers to the question of which specific parts of a region are innervated by individual axons in a different region. Reimann et al. (2019) modeled this innervation as a topographical mapping between pairs of regions in a flat view of neocortex. We used a flat map (see Sec. 4.1.1) to create a flat view of rat nbS1 subregions and recreated a matching topographical mapping between them as follows (see Fig. S2A).

First, three points were identified inside the flat view of a mouse region such that the area of the enclosed triangle is maximized. Color labels ("red", "green" and "blue") are arbitrarily assigned to the three points. Next, another three points defining a maximal area triangle were placed in the flat map of the corresponding rat region(s). The same color labels were then manually assigned to these points to best recreate their spatial context in the mouse triangle, e.g., if the point in SSp-n closest to the SSp-bfd border was labeled "red", then the point in S1ULp closest to the S1BF border will also be labeled "red". We then assume that any point in a rat region corresponds to the equally labeled point in the corresponding mouse region, with linear interpolation and extrapolation between points (Fig. S2B). This assumption transplants the existing prediction of the topographical mapping from mouse to rat, resulting in the mapping depicted in Fig. S2D. We scaled the mapping variance by a factor of 2 to account for the larger size of S1 in our rat flatmap (160 flat units) than in the mouse flatmap (80 flat units).

Finally, we derived predictions for the relative distributions of synapse locations across cortical layers for connections between subregions. Reimann et al. (2019) provided predictions for all pairs of source and target regions in mouse, which we applied to the corresponding pairs of subregions of rat nbS1. That is, we assumed these layer profiles generalize to rat, albeit using the thicker cortical layers of rats (Fig S2E1 vs. E2).

These constraints were then used to build long-range connections as described in (Reimann et al., 2019).

4.1.8 Preparation of data on thalamic inputs

As previously described in Markram et al. (2015), we aimed to add synaptic connections from thalamic regions to the circuit model. While they will ultimately serve as one of the controllable inputs for the simulation of *in vivo*-like experiments, they can also be used to make predictions of innervation strengths in our anatomical model. Specifically, we modeled two such inputs: one "bottom-up" input with a *core*-type laminar profile, and one "top-down" input with a *matrix*-type laminar profile (Harris et al., 2019; Guo et al., 2020; Shepherd and Yamawaki, 2021). In order to create biologically realistic thalamo-cortical projections with a meaningful distinction between core- and matrix-type inputs, we needed data on the strengths of these pathways and the laminar profiles of their synapses.

As in Markram et al. (2015), we used data on the cortical innervation by thalamic sources from Meyer et al. (2010), which yielded information on the depth profiles of thalamo-cortical projections. We considered data for the VPM-S1BF pathway in as representative for core-type inputs, and generalized it to all nbS1 regions (Fig. S3A1, left). Similarly, we considered data for the POm-S1BF pathway as representative of matrix-type inputs (S3A2, left), and generalized it to all nbS1 regions. Since the data is reported as absolute volumetric bouton density of thalamo-cortical axons, we were able to derive the total number of synapses to place by assuming one synapse per bouton and summing over the entire innervated volume. The depth profiles for both pathways

bioRxiv preprint doi: https://doi.org/10.1101/2022.08.11.503144; this version posted July 29, 2023. The copyright holder for this preprint (which was not certified by peer review) is the author/funder, who has granted bioRxiv a license to display the preprint in perpetuity. It is made available under aCC-BY-NC 4.0 International license.

featured two clearly separated peaks. We digitized the depth profiles and split them into 10 bins per peak. Furthermore, we applied a threshold of $0.01/\mu m^3$ below which values were set to 0 (Fig S3A).

Additionally, to constrain the innervation strength and targeting of individual thalamic axons, we used morphological reconstructions of thalamo-cortical projection neurons from the Janelia MouseLight project (mouselight.janelia.org; Economo et al. (2016)). This is a generalization of mouse data to a rat model, made necessary by the lack of a comparable resource for rat. To parameterize core-type projections, we calculated the total axonal length in somatosensory areas of $n = 11$ reconstructions with somata in VPM and axons reaching the somatosensory areas. We found lengths between 5 and 60 mm (Fig. S3 B) with a median of 27 mm that we combined with an assumed synapse density of $0.2/\mu m$ Reimann et al. (2015) to get an average number of 5400 synapses per projection fiber. To estimate of the lateral spread of the area innervated by individual axons (the vertical component is covered by the layer profiles), we considered the locations of reconstructed axon segments contained within the somatosensory regions. We then fit a Gaussian to the lateral distance of the segments from their center (Fig. S3C), resulting in a median value of $120\mu m$.

Unfortunately, the MouseLight database contained only a single neuron with soma in the POm region and axon reaching somatosensory areas (labeled as AA604), and visual inspection revealed that its axon mostly avoided these areas and to target more medial motor-related regions. As such, to parameterize the matrix-type projections, we instead calculated the lateral spread of the single axon in the motor areas ($300\mu m$ in MOp; $172\mu m$ in MOs; mean: $236\mu m$). Its total length in cortical regions was 28 mm.

4.1.9 Modeling the structure of thalamo-cortical innervation

We determined dendritic locations of thalamo-cortical input synapses as previously described in Markram et al. (2015), but adapted for the more complex geometry of this model. Briefly, binned depth profiles of densities of thalamo-cortical synapses were used as input (see Sec. 4.1.8, Fig. S9A1, A2). Next, we used the region atlas (see Sec. 4.1.1) to find the corresponding depth bins in the model. This allowed us to find all dendritic sections in the model, whose center point fell within a depth bin. We then performed a random selection of those sections and placed synapses at random locations on each selected section, until the prescribed number of synapses for a given depth bin was reached (Fig. S9A2). Sections were selected with probabilities proportional to their lengths and with replacement.

After all synapses for a thalamo-cortical projection had been placed, we mapped each of them to a presynaptic thalamic neuron. These neurons were not fully modeled, i.e., they were not assigned a soma position or morphology, the mapping simply allowed us to determine which synapses would be activated together. To parameterize the process, we used an estimate of the number of synapses formed by a single fiber and its horizontal spread (see Sec. 4.1.8). We divided the total number of synapses placed ($590 \cdot 10^6$ core-type; $380 \cdot 10^6$ matrix-type) by the number per fiber to estimate the number of innervating fibers (approximately 100'000 for the "core"-type projection; 73'000 "matrix"-type). These numbers were split between the eight subregions according to their relative volumes (Table S4), with the following steps being executed separately for each of them.

We then abstractly modeled thalamo-cortical afferent axons as lines entering their respective subregion at the bottom of layer 6 with a certain horizontal reach for the formation of synapses.

This was done by first randomly distributing locations (one per fiber) across the boundary of layers 4 and 5 (Fig. S9 B) and then moving them $1500\mu m$ along the negative voxel orientation (towards layer 6; Fig. S9 B, black dots). The resulting positions and orientation vectors were used as the starting position of the fibers and their directions, respectively (Fig. S9 B, black arrows). The presynaptic fiber of a synapse was then determined by a stochastic process based on the horizontal reach of individual fibers around their respective location (Fig. S9 B, red areas). This was parameterized as a Gaussian with a $\sigma = 120\mu m$ for core-type, and $\sigma = 235\mu m$ for matrix-type projections (see Sec. 4.1.8). For each placed synapse, its distance to neighboring fibers was

bioRxiv preprint doi: https://doi.org/10.1101/2022.08.11.503144; this version posted July 29, 2023. The copyright holder for this preprint (which was not certified by peer review) is the author/funder, who has granted bioRxiv a license to display the preprint in perpetuity. It is made available under aCC-BY-NC 4.0 International license.

calculated and used as inputs into the Gaussian (Fig. S9D). This distance was calculated as the distance between the location of the synapse and the line defined by the fiber's starting point and direction. The probability that any fiber was chosen as innervating fiber of the synapse was then proportional to the values (Fig. S9E).

4.1.10 Estimated volume of intrinsic long-range axons

As the model did not contain long-range axons, we estimated their volume based on long-range synapse counts instead. We first counted the number of long-range synapes on dendrites inside the volume of interest. We then converted the count into a volume by assuming that an axonal segment with a length of $5.4\,\mu$m and a diameter of $0.21\,\mu$m supported each synapse. The length was based on the inverse of the mean bouton density of excitatory axons in cortex (Reimann et al., 2015); the diameter was the mean diameter of axons in the model. As this excludes parts of the axon not forming boutons, this is a lower bound estimate.

4.1.11 Validation of synaptic connectivity

The part of the connectome derived with a apposition-based approach (local connectivity) was constrained by anatomical data on bouton densities and mean numbers of synapses per connection for different morphological types (Reimann et al., 2015). As such, we validated that the results match these data (Fig. S8A, B). As previously found, the only mismatch lied in the emerging bouton densities of Chandelier Cells. These neurons form synapses only onto the axon initial segment of other neurons, which we model by disregarding appositions on the dendrites. For two Chandelier types, this resulted in an insufficient number of appositions to fulfill bouton density constraints (Fig. S8A, black arrow).

Arguably the most important constraint is the number or density of excitatory synapses in pathways between individual subregions, as it determines the overall excitability of the model and the velocity of the spread of activity. Here, we compared the total number of excitatory synapses, i.e., the union of the output of both algorithms to the data (Fig. S8C), finding a robust qualitative match. Due to the stochastic nature of the connectivity algorithms, an exact match cannot be expected.

Finally, the long-range connectivity algorithm was further constrained by predicted topographical mapping between regions (Fig. S8D) and synapse layer profiles (Sec. 4.1.7E), which we validated against the data.

4.1.12 Validation of thalamo-cortical innervation

In silico synapse density profiles of VPM and POm projections were validated against the *in vitro* layer profiles from Meyer et al. (2010) that were used as the input recipes (Fig. S10A, B). To account for non-uniform thicknesses across regions, the depth values of the density profiles were normalized to the maximum thickness of each of the eight subregions. There is a decent match between the recipe and the actual layer profiles, but with a 15% overshoot at peak densities. This can be explained by the fact that the numbers of synapses to be placed were computed based on region bounding boxes which were larger than the actual volumes. Therefore, the actual densities are slightly higher when computing them on a voxel basis as it was done in this validation.

4.1.13 Calculation of common thalamic innervation

For a given thalamo-cortical pathway we calculated the common thalamic innervation (CTI) as follows for all neurons: First, for each neuron the set of thalamic fibers innervating it with at least one synapse was identified. Next, we iterated over all pairs of neurons in the model, comparing their sets of innervating fibers. Specifically, we calculated the size of the intersection of the sets and divided it by the size of their union. The resulting CTI was a measure between 0 (no overlap) and 1 (complete overlap).

bioRxiv preprint doi: https://doi.org/10.1101/2022.08.11.503144; this version posted July 29, 2023. The copyright holder for this preprint (which was not certified by peer review) is the author/funder, who has granted bioRxiv a license to display the preprint in perpetuity. It is made available under aCC-BY-NC 4.0 International license.

4.1.14 Generation of columnar subvolumes

We partitioned the modeled volume into subvolumes with shapes approximating hexagonal prisms. To that end, we represented each voxel by the flattened location of its center. In the resulting two-dimensional coordinate system, we distributed seed points in a hexagonal grid with a distance of $460\mu m$ (based on the $230\mu m$ column radius of Markram et al. (2015)) between neighboring points. Next, for each voxel we determined to which seed point it was closest. All voxels that were closest to the same seed point were then grouped together as parts of the same subvolume. As subvolumes near the periphery of the model could be incomplete, i.e., not form complete hexagonal prisms, we excluded them from further analysis if either of the following two conditions was met: 1. The subvolume had fewer than six neighbors in the hexagonal grid; 2. Its volume was less than $0.166mm^3$. That threshold is based on the volume of a circular prism with a radius of $230\mu m$ and a height of $1000\mu m$.

4.1.15 Columnar volumes and their conicality

Columnar volumes were defined in a flat view of the model, generated as in (**?**). In the two-dimensional coordinate system, we defined a hexagonal grid with a radius (large diagonal of a hexagon) as indicated in the text. Then, each voxel ($38.7348\mu m resolution$) was associated with the hexagon that contained the flat coordinates of its central point. Thus, each hexagon defined a continuous columnar volume that sampled all cortical layers. To calculate its conicality, we first found its central vertical axis (orthogonal to layer boundaries). Then we conducted a linear fit of cortical depth against distance from the vertical axis of all voxels contained in a column. The slope of the linear fit was defined as the conicality measure.

4.1.16 Generation of random connectivity control models

This section contains definitions of the random connectivity control models and explains how these were generated, presented in weakly increasing order of complexity.

The *Erdős–Rényi* controls (ER) are random directed networks where the edges are added with a fixed probability independently at random. The controls were constructed by taking each ordered pair of nodes (i, j) and adding an edge from i to j at random with probability $p = \frac{E}{N(N-1)}$, where E (respectively N) is the number of edges (respectively nodes) in the original network.

The *stochastic block model* controls (SBM) are random networks where the edges are added independently at random with a fixed probability dependent on the m-type pathway of the pre- and post-synaptic neurons. These controls were built as for the ER-controls, but with a different probability for each pathway. More precisely, if (i, j) are two neurons of m-types A and B, then their probability of connection is

$$p_{AB} = \begin{cases} \frac{E_{AB}}{(N_{AB})^2} & \text{if } A \neq B, \\ \frac{E_{AA}}{(N_{AA})(N_{AA}-1)} & \text{if } A = B, \end{cases}$$

where N_{AB} is the number of neurons of m-type A and B and E_{AB} is the number of edges from neurons of type A to neurons of type B in the original network.

The *directed configuration model* controls (CM) are random networks that closely approximate a given in/out-degree sequence, i.e., a vector of length the number of nodes, whose entries are their in/out-degrees. To build these controls, we encode the edges of the original matrix by two vectors, *sources* and *targets*, such that $(sources[i], targets[i])$ is a directed edge of the matrix (this corresponds to a binary matrix in coordinate format, useful when working with sparse matrices). Then, we shuffle the entries of both vectors *sources* and *targets* independently, which gives a new directed network, with the same degree sequence as the original. This new network might contain loops or parallel edges, so we remove them, thus this construction only approximates the original degree sequence. The density of loops and parallel edges tends to decrease as the number of nodes increases (Newman, 2003), so the approximation is good. Indeed, in our controls for local connectivity, $235,574.0 \pm 376.0$ (mean $\pm$ std) connections out of $2,050,028,490$ were missing, which is less

bioRxiv preprint doi: https://doi.org/10.1101/2022.08.11.503144; this version posted July 29, 2023. The copyright holder for this preprint (which was not certified by peer review) is the author/funder, who has granted bioRxiv a license to display the preprint in perpetuity. It is made available under aCC-BY-NC 4.0 International license.

than 0.012% of all connections. For long-range connectivity the number was $629,493.4 \pm 2,228.0$ out of $2,482,296,102$, which is less that 0.026% of all connections.

Finally, the distance block model controls (DBM) are random networks where the edges are added independently at random with a probability $p_A(d) = \alpha_A \cdot e^{-\beta_A \cdot d}$, that is, exponentially decreasing with distance d, where α_A is the probability at distance zero and β_A the decay constant, both depending only on the pre-synaptic cell m-type A. For local connectivity, the distance between a pair of neurons used was the Euclidean distance of their position in space (in μm). For long-range connectivity, the specific method used to originally construct the connectome (Reimann et al., 2019) was taken into account, preferentially connecting neurons at one location within a subregion A to neurons in another subregion B by first parameterizing linear transformations of the flattened coordinates of the two regions. The resulting *virtual coordinate system* $V_{A,B}$ is then used to connect pairs of neurons from A and B in a distance-dependent way. Therefore, the distance considered in this control between pairs of neurons was the Euclidean distance between these virtual coordinates.

For computational reasons, the model coefficients α_A and β_A were estimated by randomly sub-sampling (up to) 100 000 pre-synaptic neurons of m-type A and 100 000 post-synaptic neurons of any type and computing their pairwise distances. For local connectivity, distances from 0 to $1000\mu m$ were then divided into 20 evenly spaced $50\mu m$ bins. For long-range connectivity, distances from 0 to 400 $(a.u.)$ were divided into 20 evenly spaced 20 $(a.u.)$ bins. Connection probabilities were estimated in each bin by dividing the number of existing connections by the number of possible connections between all pairs of neurons within that bin (excluding connections at distance zero, that is, between one neuron with itself). Model coefficients were then determined by fitting the exponential probability function $p(d)$ to these data points. The whole procedure was repeated ten times with different random sub-samples of neurons, and the averaged model coefficients over these ten estimates were used to build the controls. Overall, the relative standard errors of the mean over the ten estimates were on average across all m-types less than 1%. For local connectivity, model coefficients of all 60 pre-synaptic m-types were found to be on average $\overline{\alpha} = 0.138 \pm 0.102$ (SD) and $\overline{\beta} = 0.0096 \pm 0.002$ (SD) respectively. For long-range connectivity, the model coefficients of all 18 m-types that had any outgoing long-range connections were on average $\overline{\alpha} = 0.0006 \pm 0.001$ (SD) and $\overline{\beta} = 0.012 \pm 0.001$ (SD) respectively.

4.1.17 Node participation and simplicial core

For any given node in a directed network, its *node participation* is the number of simplices that it is part of. This value can be further split by dimension, giving rise to the notion of n-node participation. Given that any directed simplex has a single source and a single target, node participation can be further refined to participation as a source or participation as a sink. For $n = 1$, source node participation is equivalent to out-degree, sink node participation is equivalent to in-degree and node participation is equivalent to the total degree (i.e., the sum of in- and out-degrees). Thus, node participation can be thought of as a higher dimensional version of degree.

The *n-simplicial core* of a network is the sub-network on the nodes that participate in simplices of dimension n or higher, or equivalently on the nodes whose n-node participation is greater than 0. The *simplicial core* is the sub-network on the nodes that participate in simplices of maximal dimension. These concepts are a generalization of the notion of core of a network, which is a notion that is solely based on degree, by taking into account higher order interactions. We refer to the (n-) simplicial core of the local/long-range network as the *(n-)local/long-range core*, and we refer to the union of both as *the core*.

4.1.18 Finding and counting simplices in connectivity networks

Directed simplices were computed using the custom-made C++ package FLAGSER-COUNT. This code is a variation of the FLAGSER package (Lütgehetmann et al., 2020). The code takes as input the adjacency matrix of a directed network in compressed sparse row (or column) format, outputs

bioRxiv preprint doi: https://doi.org/10.1101/2022.08.11.503144; this version posted July 29, 2023. The copyright holder for this preprint (which was not certified by peer review) is the author/funder, who has granted bioRxiv a license to display the preprint in perpetuity. It is made available under aCC-BY-NC 4.0 International license.

the number of directed cliques in the network, and includes the option to print all simplices. There is also the option to output node participation, so for every node v and every dimension d a value is given for the number of d-simplices that contain v. The algorithm considers each node independently as a source node and then performs a depth-first search on that node to find all simplices, where at each step it creates a new simplex by adding any node that is an out-neighbor of all nodes in the current simplex.

Since each source node is considered independently, the computations can be easily parallelized. The simplex count computations were conducted on the Blue Brain high performance computing system. Each computation was run on two Intel Xeon Gold 6248 CPUs using a total of 40 physical cores. To compute the simplex counts for the local network took 3 hours and 15 minutes using 8.2GB of memory, the long-range network took 14 hours and 44 minutes using 9.8GB of memory and the combined network took 115 days and 20 hours using 69.5GB of memory. The transpose adjacency matrices of the long-range and combined networks were used, which have the same simplex counts, because these were significantly faster to compute due to the degree distributions. The computation for the combined network was attempted on the non-transposed matrix and ran for 121 days, and computed partial counts, but encountered 898 nodes for which the counts could not be computed within 24 hours, such nodes were deemed too computational expensive and skipped.

4.1.19 Rich-club and generalized rich-club

The *k-rich-club coefficient* of an undirected network is the density of the subnetwork on the nodes of degree greater than k, and is given by the formula

$$\phi(k) = \frac{2E_{>k}}{N_{>k}(N_{>k}-1)},$$

where $N_{>k}$ is the number of nodes of degree greater than k, and $E_{>k}$ is the number of edges between the nodes in $N_{>k}$. We call the function ϕ the *rich-club curve*. For a directed network we obtain three variations of this curve depending on whether we consider in-degree, out-degree, or total-degree (the sum of in- and out-degree), and we remove the coefficient 2 due to the fact that the maximum number of edges is now $N(N-1)$ instead of $N(N-1)/2$. This gives us three formulas

$$\phi^{total}(k) = \frac{E^{total}_{>k}}{N^{total}_{>k}(N^{total}_{>k}-1)}, \quad \phi^{in}(k) = \frac{E^{in}_{>k}}{N^{in}_{>k}(N^{in}_{>k}-1)}, \quad \phi^{out}(k) = \frac{E^{out}_{>k}}{N^{out}_{>k}(N^{out}_{>k}-1)}, \tag{1}$$

where $N^{total}_{>k}$ (resp. $E^{total}_{>k}$) is equivalent to $N_{>k}$ (resp. $E_{>k}$) but restricted to the total degree, and similarly for in and out.

The rich-club coefficient can be naturally generalized by replacing the degree with any network metric (Opsahl et al., 2008). In particular, we define the *simplicial rich-club coefficient* by

$$\phi^{d}(k) = \frac{E^{d}_{>k}}{N^{d}_{>k}(N^{d}_{>k}-1)}, \tag{2}$$

where $N^{d}_{>k}$ is the number of nodes with d-node participation at least k, and $E^{d}_{>k}$ is the number of edges between them. Note that $\phi^1 = \phi^{total}$ since a 1-simplex is simply an edge of the network.

A large rich-club coefficient value is said to indicate a preference of high degree nodes to connect together. However, it is shown in Colizza et al. (2006) that the rich-club coefficient is increasing even in Erdős–Rényi networks, and is actually a consequence of higher degree nodes naturally being more likely to connect. Therefore, it is important to normalize the rich-club coefficient by dividing by the rich-club of an appropriate control, that is, a control with the same degree distribution such as a configuration model, see Section 4.1.16. Hence we define the *normalized rich-club coefficient* as

$$\rho^{total}(k) = \frac{\phi^{total}(k)}{\phi^{total}_{rand}(k)}, \tag{3}$$

bioRxiv preprint doi: https://doi.org/10.1101/2022.08.11.503144; this version posted July 29, 2023. The copyright holder for this preprint (which was not certified by peer review) is the author/funder, who has granted bioRxiv a license to display the preprint in perpetuity. It is made available under aCC-BY-NC 4.0 International license.

where $\phi^{total}_{rand}(k)$ is the rich-club coefficient of a configuration model control of the original network, and we similarly define $\rho^{in}(k)$ and $\rho^{out}(k)$. A network is said to have a *rich-club effect* if $\rho^{total}(k) > 1$, as this indicates the high degree nodes connect together more than is "expected". The importance of this normalization can be seen in Figure S11, where B1 seems to indicate the presence of a rich-club effect for the long-range network, which disappears when normalized in B2.

Normalizing the simplicial rich-club is difficult as it requires a control model on directed flag complexes that fixes node participation. Randomly sampling simplicial complexes with fixed simplex counts or other high dimensional network properties is an active area of research (Kahle et al., 2014; Young et al., 2017; Unger and Krebs, 2022), but as of yet there is no known appropriate control model for the simplicial rich-club, and it is a topic that warrants further investigation.

4.1.20 Paths and path distances

Let G be a directed network on n nodes, with adjacency matrix A. A *path* of length k (or k-path) from node u to node v is a sequence of nodes $u = x_1, \ldots, x_{k+1} = v$ such that (x_i, x_{i+1}) is an edge of G for all $i = 1, \ldots, k$. The *path distance* between u and v is the length of the shortest path from u to v. A path from u to v is *geodesic* if its length is the path distance from u to v.

The number of k-paths between all nodes in G can be easily computed using matrix multiplication, since the number of k-paths between u and v is given by $A^k_{u,v}$, where A is the adjacency matrix of G (Diestel, 2005). Consequently, the number of k-paths from the nodes $i_1, \ldots, i_t$ to all other nodes in G is given by

$$A^k_{[i_1,\ldots,i_t]} = A_{[i_1,\ldots,i_t]}A^{k-1} = A^{k-1}_{[i_1,\ldots,i_t]}A,$$

where $A_{[i_1,\ldots,i_t]}$ is the $t \times n$ matrix obtained from A by taking only the rows $i_1, \ldots, i_t$. Note that the smallest k for which entry i, j is nonzero is the path distance from i to j.

Using this approach we were able to compute the path distances in the combined network between pairs of all 396 nodes in the local and long-range cores. We ran the computation in parallel by partitioning the nodes into 13 sets $C_1, \ldots, C_{13}$ of approximately 23 nodes each and computing

$$A^k_{[C_i]} = (\ldots(A_{[C_i]}\underbrace{A)A)\ldots A}_{\times k-1}).$$

Note that the order of the brackets ensures that at each step a 23×4234929 matrix is computed, rather than a 4234929×4234929 matrix.

Once we had the path distances between the nodes in the local and long-range cores, we computed the geodesic paths between them. This was done using the custom C++ package PATHFINDER. This code functions in a similar way to FLAGSER-COUNT, except that at each step it creates a new path by considering any node that is an out-neighbor of the final node in the current path. At input the start-nodes, end-nodes, and path distances can be specified. To compute all geodesic paths of length at most three between nodes within the local and long-range cores took 8 hours and 47 minutes, using 51.9GB of memory. Between these 396 nodes there are $6,383$ geodesic 1-paths, $1,039,814$ geodesic 2-paths, and $21,701,345$ geodesic 3-paths. To compute all geodesic 4-paths was attempted, but after running for 24 hours failed to finish, and is likely to be computationally infeasible due to the exponential growth of the number of paths.

4.1.21 Generation of EM-like volumes

We emulated the specificities of the electron microscopic studies of Motta et al., 2019 and Schneider-Mizell et al., 2023 as follows. First, in Motta et al., 2019 the fragments of axons and dendrites inside a volume are reconstructed as well as their synaptic connections. Then, axon and dendrite fragments with at least 10 synapses inside the volume are considered for analysis. In the model, we began by loading the three-dimensional locations of all synapses between neurons in a $100\mu m$ columnar volume. Next, we determined which synapses are contained in a box-shaped subvolume at the top of layer 4 of the model. The size of the box was determined to contain the same number

bioRxiv preprint doi: https://doi.org/10.1101/2022.08.11.503144; this version posted July 29, 2023. The copyright holder for this preprint (which was not certified by peer review) is the author/funder, who has granted bioRxiv a license to display the preprint in perpetuity. It is made available under aCC-BY-NC 4.0 International license.

of synapses (approximately 145'000) as the volume of Motta et al., 2019. This was achieved at $110x110x85\mu m$, about twice as large as the reference volume, as it does not contain synapses extrinsic to the model (also we do not know to what degree the dimensions of the reference volume were corrected for shrinkage). We then determined the types of postsynaptic compartments. Synapses onto somata and axon initial segments were labeled as such; of the rest, if the soma of the targeted neuron was inside the box volume, it was tagged as proximal dendrite; of the rest, if the targeted neuron was inhibitory, it was tagged as smooth dendrite; remaining synapses onto apical dendrites were tagged as such; all others were tagged "other". We applied the same filtering as the reference, removing axons, dendrites (and their synapses) with less than 10 synaptic contacts.

On the other hand, Schneider-Mizell et al., 2023 determined which neurons had their somata inside a volume, and then reconstructed their entire dendritic and axonal trees, even parts outside the volume. The volume sampled all layers and was approximately $100x100\mu m$ wide, but was not exactly box-shaped, as it followed the main direction of contained apical dendrites. We emulated this by defining a subvolume in flat mapped coordinates (Bolaños-Puchet and Reimann, prep): We considered all neurons whose flattened coordinates were inside a $100x100\mu m$ square. As the flat map flattens away the vertical dimension along which apical dendrites are oriented in the model, this corresponded to the the sampling of Schneider-Mizell et al., 2023. Then, all synaptic connections between the sampled neurons were analyzed as in the reference.

4.1.22 Binomial "first hit" model

Control models to compare the distributions of postsynaptic compartments against were generated as described in the reference (Motta et al., 2019). The binomial model assumes that each synapse of an axon is formed with a fixed probability p_{type} onto a given postsynaptic compartment type, hence the expected distribution of the number of synapses onto that type is a binomial one. A binomial model is fitted for each combination of axon type (excitatory vs. inhibitory) and postsynaptic compartment type as follows. For all axon fragments of the given type, we consider the total number of synapses formed and whether it forms at least one synapse onto the given compartment type. For a given axon fragment, the likelihood of the observation is $(1-p_{type})^{n_{axon}}$ if no synapse onto the type is observed and $1-(1-p_{type})^{n_{axon}}$ otherwise, where n_{axon} is the number of synapses of the axon fragment in the volume. Then, p_{type} is estimated by maximizing the joint likelihood of all observations, i.e. over all axons of the given type.

bioRxiv preprint doi: https://doi.org/10.1101/2022.08.11.503144; this version posted July 29, 2023. The copyright holder for this preprint (which was not certified by peer review) is the author/funder, who has granted bioRxiv a license to display the preprint in perpetuity. It is made available under aCC-BY-NC 4.0 International license.

Author contributions

- Conceptualization: H.M., E.B.M., S.R., M.W.R.
- Data curation: Y.S., W.V.G., S.B.P., H.L., D.K., L.K.
- Formal analysis: L.K., S.B.P., A.E., D.E.S., M.W.R.
- Funding acquisition: H.M.
- Investigation: D.E.S., M.W.R., J.P.S., M.S.
- Methodology: E.B.M, L.K., W.V.G, S.R., S.B.P., A.R., D.E.S., N.N., M.W.R., K.H., J.L., R.L., J.P.S., D.K.
- Project administration: H.M., F.S., E.B.M, S.R., A.R., M.W.R., K.H., R.L., S.L., J.P.
- Resources: F.S., J.K., P.K., F.P., J.-D.C.
- Software: A.A., H.D., V.S., S.B.P, A.E., M.W.R., H.L., J.L., J.P.S., F.D., A.De., J.K., P.K., F.P., M.W., B.C., J.-D.C., T.D., G.F., M.G., J.B.H., L.V., J.H., J.L.R.
- Supervision: H.M., F.S., E.B.M, S.R., A.R., M.W.R., K.H., R.L., J.K., J.-D.C.
- Validation: L.K., W.V.G, H.D., V.S., S.B.P, A.E., C.P., M.W.R., A.Di., M.G.
- Visualization: L.K., S.B.P, A.E., D.E.S., J.L., C.P., M.W.R., C.F.
- Writing - original draft: S.B.P, D.E.S., L.K., C.P., J.P.S., M.W.R., D.K., M.S.
- Writing - review & editing: A.A., S.B.P., S.R., A.E., J.I., M.W.R., K.H., R.L.

Acknowledgements

The authors would like to thank Giuseppe Chindemi, Javier DeFelipe and Rajnish Ranjan for help with the scientific development of the model; Tristan Carel, James Dynes, Stefan Eilemann, Bruno Magalhães, Juan Hernando Vieites and Arseny Povolotsky for contributions and support to the engineering challenges; the BBP Core Services team for responding to IT requests and services surrounding the research; Marwan Abdellah, Elvis Boci and Nadir Roman Guerrero for help with visualizations of the model; Zoltán Kisvárday for supervision of morphology reconstruction efforts; Eva Kenny, Silvia Scarabelli and Riccardo Sinsi for help with project management; and Karin Holm, Akiko Sato and Georges Khazen for support of manuscript development and helpful discussions.

Funding

This study was supported by funding to the Blue Brain Project, a research center of the École polytechnique fédérale de Lausanne (EPFL), from the Swiss government's ETH Board of the Swiss Federal Institutes of Technology. RL, JPS and JL were supported by EPSRC under grant number EP/P025072/1. RL was supported by a collaboration grant from EPFL.

bioRxiv preprint doi: https://doi.org/10.1101/2022.08.11.503144; this version posted July 29, 2023. The copyright holder for this preprint (which was not certified by peer review) is the author/funder, who has granted bioRxiv a license to display the preprint in perpetuity. It is made available under aCC-BY-NC 4.0 International license.

References

Abdellah, M., Hernando, J., Eilemann, S., Lapere, S., Antille, N., Markram, H., and Schürmann, F. (2018). NeuroMorphoVis: A collaborative framework for analysis and visualization of neuronal morphology skeletons reconstructed from microscopy stacks. *Bioinformatics*, 34(13):i574–i582.

Anwar, H., Riachi, I., Hill, S., Schürmann, F., and Markram, H. (2009). An Approach to Capturing Neuron Morphological Diversity. In De Schutter, E., editor, *Computational Modeling Methods for Neuroscientists*, pages 211–232. The MIT Press.

Barabási, D. L., Bianconi, G., Bullmore, E., Burgess, M., Chung, S., Eliassi-Rad, T., George, D., Kovács, I. A., Makse, H., Papadimitriou, C., et al. (2023). Neuroscience needs network science. *arXiv preprint arXiv:2305.06160*.

Billeh, Y. N., Cai, B., Gratiy, S. L., Dai, K., Iyer, R., Gouwens, N. W., Abbasi-Asl, R., Jia, X., Siegle, J. H., Olsen, S. R., et al. (2020). Systematic integration of structural and functional data into multi-scale models of mouse primary visual cortex. *Neuron*, 106(3):388–403.

Bolaños-Puchet, S. and Reimann, M. W. (prep). Flattening of enhanced cortical atlases opens up new possibilities for data-driven modeling and data visualization. *In preparation*.

Bota, M., Sporns, O., and Swanson, L. W. (2015). Architecture of the cerebral cortical association connectome underlying cognition. *Proceedings of the National Academy of Sciences*, 112(16).

Buzás, P., Eysel, U. T., and Kisvárday, Z. F. (1998). Functional topography of single cortical cells: an intracellular approach combined with optical imaging. *Brain research. Brain research protocols*, 3 2:199–208.

Colizza, V., Flammini, A., Serrano, M. A., and Vespignani, A. (2006). Detecting rich-club ordering in complex networks. *Nature physics*, 2(2):110–115.

Curto, C., Giusti, C., Marku, K., Pastalkova, E., and Itskov, V. (2013). Pairwise correlation graphs from hippocampal population activity have highly non-random, low-dimensional clique topology. *BMC neuroscience*, 14(1):1–2.

Dai, K., Hernando, J., Billeh, Y. N., Gratiy, S. L., Planas, J., Davison, A. P., Dura-Bernal, S., Gleeson, P., Devresse, A., Dichter, B. K., et al. (2020). The sonata data format for efficient description of large-scale network models. *PLoS computational biology*, 16(2):e1007696.

Diestel, R. (2005). Graph theory 3rd ed. *Graduate texts in mathematics*, 173:33.

Ecker, A., Santander, D. E., Bolaños-Puchet, S., Isbister, J. B., and Reimann, M. W. (2023). Cortical cell assemblies and their underlying connectivity: an in silico study. *bioRxiv*, pages 2023–02.

Economo, M. N., Clack, N. G., Lavis, L. D., Gerfen, C. R., Svoboda, K., Myers, E. W., and Chandrashekar, J. (2016). A platform for brain-wide imaging and reconstruction of individual neurons. *eLife*, 5:e10566.

Fares, T. and Stepanyants, A. (2009). Cooperative synapse formation in the neocortex. *Proceedings of the National Academy of Sciences*, 106(38):16463–16468.

Felleman, D. J. and Van Essen, D. C. (1991). Distributed hierarchical processing in the primate cerebral cortex. *Cerebral Cortex (New York, N.Y.: 1991)*, 1(1):1–47.

Gal, E., London, M., Globerson, A., Ramaswamy, S., Reimann, M. W., Muller, E., Markram, H., and Segev, I. (2017). Rich cell-type-specific network topology in neocortical microcircuitry. *Nature Neuroscience*, 20(7):1004–1013.

Gal, E., Perin, R., Markram, H., London, M., and Segev, I. (2020). Neuron geometry underlies universal network features in cortical microcircuits. *bioRxiv*.

Garey, L. (1999). Cortex: Statistics and geometry of neuronal connectivity, 2nd edn. by v. braitenberg and a. schüz.(pp. xiii+ 249; 90 figures; isbn 3 540 63816 4). berlin: Springer. 1998. *The Journal of Anatomy*, 194(1):153–157.

Gerfen, C. R., Economo, M. N., and Chandrashekar, J. (2018). Long distance projections of cortical pyramidal neurons. *Journal of Neuroscience Research*, 96(9):1467–1475.

Ghobril, J.-P. (2015). *Doctoral Dissertation: Large Volume Imaging of Rodent Brain Anatomy with Emphasis on Selective Plane Illumination Microscopy*. École polytechnique fédérale de Lausanne.

Giacopelli, G., Tegolo, D., Spera, E., and Migliore, M. (2021). On the structural connectivity of large-scale models of brain networks at cellular level. *Scientific Reports*, 11(1):4345.

Giusti, C., Pastalkova, E., Curto, C., and Itskov, V. (2015). Clique topology reveals intrinsic geometric structure in neural correlations. *Proceedings of the National Academy of Sciences*, 112(44):13455–13460.

bioRxiv preprint doi: https://doi.org/10.1101/2022.08.11.503144; this version posted July 29, 2023. The copyright holder for this preprint (which was not certified by peer review) is the author/funder, who has granted bioRxiv a license to display the preprint in perpetuity. It is made available under aCC-BY-NC 4.0 International license.

Guo, K. H., Yamawaki, N., Barrett, J. M., Tapies, M., and Shepherd, G. M. (2020). Cortico-thalamo-cortical circuits of mouse forelimb S1 are organized primarily as recurrent loops. *Journal of Neuroscience*, 40(14):2849–2858.

Harris, J. A., Mihalas, S., et al. (2019). Hierarchical organization of cortical and thalamic connectivity. *Nature*, 575(7781):195–202.

Hill, S. L., Wang, Y., Riachi, I., Schürmann, F., and Markram, H. (2012). Statistical connectivity provides a sufficient foundation for specific functional connectivity in neocortical neural microcircuits. *Proceedings of the National Academy of Sciences*, 109(42):E2885–E2894.

Kahle, M. (2009). Topology of random clique complexes. *Discrete mathematics*, 309(6):1658–1671.

Kahle, M. et al. (2014). Topology of random simplicial complexes: a survey. *AMS Contemp. Math*, 620:201–222.

Kanari, L., Dłotko, P., Scolamiero, M., Levi, R., Shillcock, J., Hess, K., and Markram, H. (2018). A topological representation of branching neuronal morphologies. *Neuroinformatics*, 16(1):3–13.

Kanari, L., Ramaswamy, S., Shi, Y., Morand, S., Meystre, J., Perin, R., Abdellah, M., Wang, Y., Hess, K., and Markram, H. (2019). Objective Morphological Classification of Neocortical Pyramidal Cells. *Cerebral Cortex*, 29(4):1719–1735.

Karube, F. and Kisvárday, Z. F. (2011). Axon topography of layer iv spiny cells to orientation map in the cat primary visual cortex (area 18). *Cerebral cortex*, 21 6:1443–58.

Keller, D., Meystre, J., Veettil, R. V., Burri, O., Guiet, R., Schürmann, F., and Markram, H. (2019). A Derived Positional Mapping of Inhibitory Subtypes in the Somatosensory Cortex. *Frontiers in Neuroanatomy*, 13(78).

Lütgehetmann, D., Govc, D., Smith, J. P., and Levi, R. (2020). Computing Persistent Homology of Directed Flag Complexes. *Algorithms*, 13(1):19.

Markram, H., Muller, E. B., Ramaswamy, S., Reimann, M. W., et al. (2015). Reconstruction and Simulation of Neocortical Microcircuitry. *Cell*, 163:456–492.

Meyer, H. S., Wimmer, V. C., Hemberger, M., Bruno, R. M., De Kock, C. P., Frick, A., Sakmann, B., and Helmstaedter, M. (2010). Cell type-specific thalamic innervation in a column of rat vibrissal cortex. *Cerebral Cortex*, 20(10):2287–2303.

MICrONS-Consortium, Bae, J. A., Baptiste, M., Bishop, C. A., Bodor, A. L., Brittain, D., Buchanan, J., Bumbarger, D. J., Castro, M. A., Celii, B., et al. (2021). Functional connectomics spanning multiple areas of mouse visual cortex. *BioRxiv*, pages 2021–07.

Mishchenko, Y., Hu, T., Spacek, J., Mendenhall, J., Harris, K. M., and Chklovskii, D. B. (2010). Ultrastructural analysis of hippocampal neuropil from the connectomics perspective. *Neuron*, 67(6):1009–1020.

Motta, A., Berning, M., Boergens, K. M., Staffler, B., Beining, M., Loomba, S., Hennig, P., Wissler, H., and Helmstaedter, M. (2019). Dense connectomic reconstruction in layer 4 of the somatosensory cortex. *Science*, 366(6469):eaay3134.

Muralidhar, S., Wang, Y., and Markram, H. (2014). Synaptic and cellular organization of layer 1 of the developing rat somatosensory cortex. *Frontiers in Neuroanatomy*, 7.

Newman, M. E. J. (2003). The Structure and Function of Complex Networks. *SIAM Review*, 45(2):167–256.

Oh, S. W., Harris, J. A., Ng, L., Winslow, B., Cain, N., Mihalas, S., Wang, Q., Lau, C., Kuan, L., Henry, A. M., Mortrud, M. T., Ouellette, B., Nguyen, T. N., Sorensen, S. A., Slaughterbeck, C. R., Wakeman, W., Li, Y., Feng, D., Ho, A., Nicholas, E., Hirokawa, K. E., Bohn, P., Joines, K. M., Peng, H., Hawrylycz, M. J., Phillips, J. W., Hohmann, J. G., Wohnoutka, P., Gerfen, C. R., Koch, C., Bernard, A., Dang, C., Jones, A. R., and Zeng, H. (2014). A mesoscale connectome of the mouse brain. *Nature*, 508(7495):207–214.

Opsahl, T., Colizza, V., Panzarasa, P., and Ramasco, J. J. (2008). Prominence and control: the weighted rich-club effect. *Physical review letters*, 101(16):168702.

Paxinos, G. and Watson, C. (2007). *The Rat Brain in Stereotaxic Coordinates (Sixth Edition)*. Academic Press, London.

Peters, A. and Feldman, M. L. (1976). The projection of the lateral geniculate nucleus to area 17 of the rat cerebral cortex. i. general description. *Journal of neurocytology*, 5(1):63–84.

Rees, C. L., Moradi, K., and Ascoli, G. A. (2017). Weighing the evidence in peters' rule: does neuronal morphology predict connectivity? *Trends in neurosciences*, 40(2):63–71.

Reimann, M. W., Gevaert, M., Shi, Y., Lu, H., Markram, H., and Muller, E. (2019). A null model of the mouse whole-neocortex micro-connectome. *Nature Communications*, 10(3903).

bioRxiv preprint doi: https://doi.org/10.1101/2022.08.11.503144; this version posted July 29, 2023. The copyright holder for this preprint (which was not certified by peer review) is the author/funder, who has granted bioRxiv a license to display the preprint in perpetuity. It is made available under aCC-BY-NC 4.0 International license.

Reimann, M. W., Horlemann, A.-L., Ramaswamy, S., Muller, E. B., and Markram, H. (2017a). Morphological diversity strongly constrains synaptic connectivity and plasticity. *Cerebral Cortex*, 27(9):4570–4585.

Reimann, M. W., King, J. G., Muller, E. B., Ramaswamy, S., and Markram, H. (2015). An algorithm to predict the connectome of neural microcircuits. *Frontiers in computational neuroscience*, 9(120).

Reimann, M. W., Nolte, M., Scolamiero, M., Turner, K., Perin, R., Chindemi, G., Dłotko, P., Levi, R., Hess, K., and Markram, H. (2017b). Cliques of neurons bound into cavities provide a missing link between structure and function. *Frontiers in Computational Neuroscience*, 11(48).

Romani, A., Antonietti, A., Bella, D., Budd, J., Giacalone, E., Kurban, K., Saray, S., Abdellah, M., Arnaudon, A., Boci, E., et al. (2023). Community-based reconstruction and simulation of a full-scale model of region ca1 of rat hippocampus. *bioRxiv*, pages 2023–05.

Ronan, L., Pienaar, R., Williams, G., Bullmore, E., Crow, T. J., Roberts, N., Jones, P. B., Suckling, J., and Fletcher, P. C. (2011). Intrinsic curvature: a marker of millimeter-scale tangential cortico-cortical connectivity? *International journal of neural systems*, 21(05):351–366.

Santuy, A., Turégano-López, M., Rodríguez, J. R., Alonso-Nanclares, L., DeFelipe, J., and Merchán-Pérez, A. (2018). A Quantitative Study on the Distribution of Mitochondria in the Neuropil of the Juvenile Rat Somatosensory Cortex. *Cerebral Cortex*, 28(10):3673–3684.

Scannell, J., Blakemore, C., and Young, M. (1995). Analysis of connectivity in the cat cerebral cortex. *The Journal of Neuroscience*, 15(2):1463–1483.

Schneider-Mizell, C. M., Bodor, A., Brittain, D., Buchanan, J., Bumbarger, D. J., Elabbady, L., Kapner, D., Kinn, S., Mahalingam, G., Seshamani, S., et al. (2023). Cell-type-specific inhibitory circuitry from a connectomic census of mouse visual cortex. *bioRxiv*, pages 2023–01.

Scholtens, L. H., Schmidt, R., de Reus, M. A., and van den Heuvel, M. P. (2014). Linking Macroscale Graph Analytical Organization to Microscale Neuroarchitectonics in the Macaque Connectome. *Journal of Neuroscience*, 34(36):12192–12205.

Schüz, A. and Palm, G. (1989). Density of neurons and synapses in the cerebral cortex of the mouse: NEURONS AND SYNAPSES IN THE MOUSE CORTEX. *Journal of Comparative Neurology*, 286(4):442–455.

Shepherd, G. M. and Yamawaki, N. (2021). Untangling the cortico-thalamo-cortical loop: cellular pieces of a knotty circuit puzzle. *Nature Reviews Neuroscience*, 22(7):389–406.

Sizemore, A. E., Giusti, C., Kahn, A., Vettel, J. M., Betzel, R. F., and Bassett, D. S. (2018). Cliques and cavities in the human connectome. *Journal of Computational Neuroscience*, 44(1):115–145.

Somogyi, P. and Freund, T. F. (1989). Immunocytochemistry and Synaptic Relationships of Physiologically Characterized HRP-Filled Neurons. In Heimer, L. and Záborszky, L., editors, *Neuroanatomical Tract-Tracing Methods 2*, pages 239–264. Springer US, Boston, MA.

Storey, J. D. and Tibshirani, R. (2003). Statistical significance for genomewide studies. *Proceedings of the National Academy of Sciences*, 100(16):9440–9445.

Toledo-Rodriguez, M., Goodman, P., Illic, M., Wu, C., and Markram, H. (2005). Neuropeptide and calcium-binding protein gene expression profiles predict neuronal anatomical type in the juvenile rat. *Journal of Physiology*, 567(2):401–413.

Towlson, E. K., Vértes, P. E., Ahnert, S. E., Schafer, W. R., and Bullmore, E. T. (2013). The rich club of the c. elegans neuronal connectome. *Journal of Neuroscience*, 33(15):6380–6387.

Tremblay, R., Lee, S., and Rudy, B. (2016). Gabaergic interneurons in the neocortex: from cellular properties to circuits. *Neuron*, 91(2):260–292.

Unger, F. and Krebs, J. (2022). Mcmc sampling of directed flag complexes. *In preparation*.

van den Heuvel, M. P. and Sporns, O. (2011). Rich-Club Organization of the Human Connectome. *Journal of Neuroscience*, 31(44):15775–15786.

Young, J.-G., Petri, G., Vaccarino, F., and Patania, A. (2017). Construction of and efficient sampling from the simplicial configuration model. *Physical Review E*, 96(3):032312.

Zhou, S. and Mondragon, R. (2004). The Rich-Club Phenomenon in the Internet Topology. *IEEE Communications Letters*, 8(3):180–182.

bioRxiv preprint doi: https://doi.org/10.1101/2022.08.11.503144; this version posted July 29, 2023. The copyright holder for this preprint (which was not certified by peer review) is the author/funder, who has granted bioRxiv a license to display the preprint in perpetuity. It is made available under aCC-BY-NC 4.0 International license.

5 Supplementary Material

5.1 Results of individual validations

We began by validating that the cortical layers placed in the atlas formed a stack of continuous volumes. To that end, we calculated the fraction of voxels in each layer that were directly adjacent to another layer. As expected, adjacent voxels were found only between adjacent layers. Fractions of adjacent voxels decreased in lower layers as they are generally thicker and due to the curved geometry of the volume. Additionally, we tested that layers are spatially continuous by confirming that for each voxel there was at least one neighboring voxel in the same layer. This was the case for over 99.99% of the voxels with the handful of violating voxels limited to the periphery of the modeled volume (not shown).

To validate the neuronal composition of the model, we then compared the densities of excitatory and inhibitory neurons placed in the model against the input constraints. The vertical density profiles matched the input robustly, with minor numerical differences resulting from the need to round the number of neurons to place in a voxel to the nearest integer.

The biologically correct placement of neuronal morphologies was first validated by visual inspection of renderings of neurons in the context of the atlas (Figure S7). More quantitatively, we considered for each neuron its *placement score* that quantifies to what degree manually identified morphological features reach the correct layers and neurites remain within the model volume (see Figure S6; STAR*Methods). Specifically, we ensured that the fraction of neurons with poor placement score remained below 1%.

Connectivity was validated in terms of the following aspects: We ensured that the mean bouton density on axons matched biological reference data (Figure S8A). A mismatch was only observed for Chandelier Cells in layers 2/3 and 4. This is a consequence of the highly specific connectivity of those m-types targeting only axon initial segments of postsynaptic neurons, which is challenging to model based on axonal appositions. Further, we ensured that the mean number of synapses per connection in m-type-specific pathways matches the biological reference (Figure S8B). For long-range connectivity, we ensured that the topographical mapping between subregions and laminar profiles of synapse locations matches the specified references (Figure S8D, E). For the union of local and long-range connectivity, we validated the overall density of synaptic connections between subregions (Figure S8C). Finally, for thalamic inputs we validated their overall strengths and layer specificities by comparing the laminar profiles of their synapse locations to reference data (Figure S10).

5.2 List of assumptions made in model building

Inherited assumptions
We assume that the published data sources and modelling steps (Table 1) are correct and consequently inherit their assumptions. Below, we will only list the assumptions made on top of that.

Data assumptions
We make a number assumptions related to generalizing input data

- We assume the juvenile rat SSCx volume is a uniformly scaled-down version of the adult SSCx.
- We assume no significant variability between nbS1 regions in terms of: Cell density layer profiles, neuronal morphologies, bouton densities, number of synapses per connection in pathways.
- We assume the relative strengths of connectivity and structure axonal targeting is comparable in SSCx regions between mouse and rat.

bioRxiv preprint doi: https://doi.org/10.1101/2022.08.11.503144; this version posted July 29, 2023. The copyright holder for this preprint (which was not certified by peer review) is the author/funder, who has granted bioRxiv a license to display the preprint in perpetuity. It is made available under aCC-BY-NC 4.0 International license.

- We assume that the VPM to barrel cortex projection in adult rat is representative for a general core-type, feedforward thalamic input in juvenile rat. Similarly, POm to barrel cortex for matrix-type, feedback input.
- We assume mouse thalamo-cortical projection axons are informative for the structure of the rat thalamo-cortical projection system.

Structuring assumptions

- We assume that grouping of cortical neurons into 60 morphological classes is also useful for the description of the neuronal composition (cell density profiles) and the synaptic connectivity between them.
- We assume that the eight established subregions provide a parcellation that is useful for the description of long-range connectivity in the model.

Modeling assumption

- We assume that purely vertical cell density profiles capture all relevant details of neuronal composition.
- We assume that the union of synaptic connections from two separate algorithms accurately describes the connectivity at all scales that are relevant in the model. Specifically, we assume there is no "midrange gap" remaining between the two algorithms.
- We assume that thalamo-cortical axons do not target specific classes of neurons, beyond what is given by their layer profiles.
- We assume the horizontal spread of thalamo-cortical axons can be captured by a Gaussian profile for the synapses formed.

5.3 Supplementary Tables and Figures

bioRxiv preprint doi: https://doi.org/10.1101/2022.08.11.503144; this version posted July 29, 2023. The copyright holder for this preprint (which was not certified by peer review) is the author/funder, who has granted bioRxiv a license to display the preprint in perpetuity. It is made available under aCC-BY-NC 4.0 International license.

Table S1: Morphological types (m-types) used in the model

L1_DAC	Layer 1, descending axon cell	L1_HAC	Layer 1, horizontal axon cell
L1_LAC		L1_NGC-DA	
L1_NGC-SA		L1_SAC	
L23_BP	Layer 2, bipolar cell	L23_BTC	Layer 2/3, bitufted cell
L23_CHC	Layer 2/3, chandelier cell	L23_DBC	Layer 2/3, double bouquet cell
L23_LBC	Layer 2/3, large basket cell	L23_MC	Layer 2/3, martinotti cell
L23_NBC	Layer 2/3, nest basket cell	L23_NGC	Layer 2/3, neurogliaform cell
L23_SBC	Layer 2/3, small basket cell	L2_IPC	Layer 2, inverted pyramidal cell
L2_TPC:A	Layer 2, large tufted pyramidal cell	L2_TPC:B	Layer 2, early bifurcating pyramidal cell
L3_TPC:A	Layer 3, large tufted pyramidal cell	L3_TPC:C	Layer 3, small tufted pyramidal cell
L4_BP	Layer 4, bipolar cell	L4_BTC	Layer 4, bitufted cell
L4_CHC	Layer 4, chandelier cell	L4_DBC	Layer 4, double bouquet cell
L4_LBC	Layer 4, large basket cell	L4_MC	Layer 4, martinotti cell
L4_NBC	Layer 4, nest basket cell	L4_NGC	Layer 4, neurogliaform cell
L4_SBC	Layer 4, small basket cell	L4_SSC	Layer 4, spiny stellate cell
L4_TPC	Layer 4, tufted pyramidal cell	L4_UPC	Layer 4, untufted pyramidal cell
L5_BP	Layer 5, bipolar cell	L5_BTC	Layer 5, bitufted cell
L5_CHC	Layer 5, chandelier cell	L5_DBC	Layer 5, double bouquet cell
L5_LBC	Layer 5, large basket cell	L5_MC	Layer 5, martinotti cell
L5_NBC	Layer 5, nest basket cell	L5_NGC	Layer 5, neurogliaform cell
L5_SBC	Layer 5, small basket cell	L5_TPC:A	Layer 5, large tufted pyramidal cell
L5_TPC:B	Layer 5, early bifurcating pyramidal cell	L5_TPC:C	Layer 5, small tufted pyramidal cell
L5_UPC	Layer 5, untufted pyramidal cell	L6_BP	Layer 6, bipolar cell
L6_BPC	Layer 6 bipolar cell	L6_BTC	Layer 6, bitufted cell
L6_CHC	Layer 6, chandelier cell	L6_DBC	Layer 6, double bouquet cell
L6_HPC	Layer 6, horizontal pyramidal cell	L6_IPC	Layer 6, inverted pyramidal cell
L6_LBC	Layer 6, large baskte cell	L6_MC	Layer 6, martinotti cell
L6_NBC	Layer 6, nest basket cell	L6_NGC	Layer 6, neurogliaform cell
L6_SBC	Layer 6, small basket cell	L6_TPC:A	Layer 6, large tufted pyramidal cell
L6_TPC:C	Layer 6, small tufted pyramidal cell	L6_UPC	Layer 6 untufted pyramidal cell

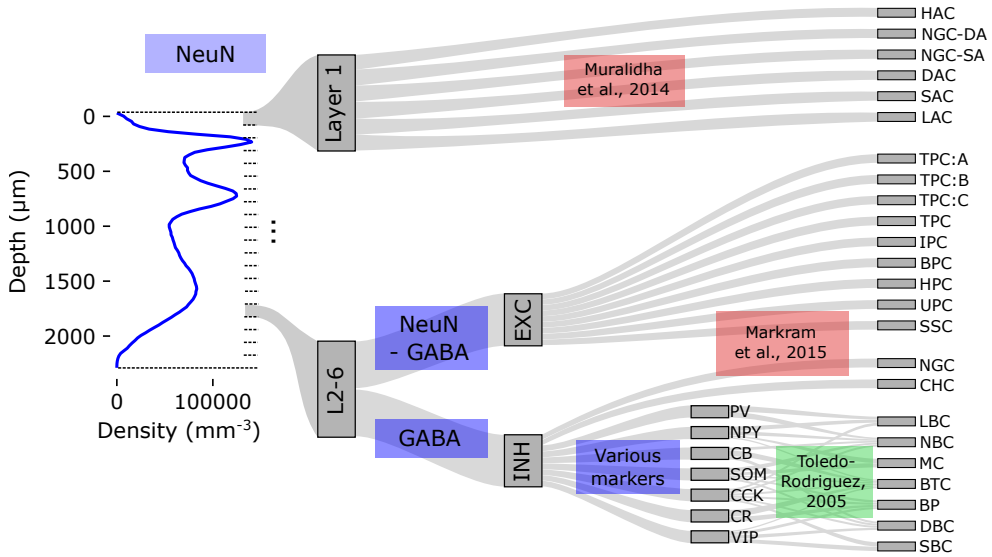

Figure S1: Derivation of neuron density depth profiles. Left: A vertical profile of neuron densities, calculated from antibody stains of neuronal nuclear protein (NeuN). From left to right: Neuron densities in each bin are split into individual morphological types through antibody stains for various markers (blue boxes) and an established mapping of markers to types (green), or by applying established neuronal compositions (red). Information in this flow diagram is illustrative, not quantitative.

bioRxiv preprint doi: https://doi.org/10.1101/2022.08.11.503144; this version posted July 29, 2023. The copyright holder for this preprint (which was not certified by peer review) is the author/funder, who has granted bioRxiv a license to display the preprint in perpetuity. It is made available under aCC-BY-NC 4.0 International license.

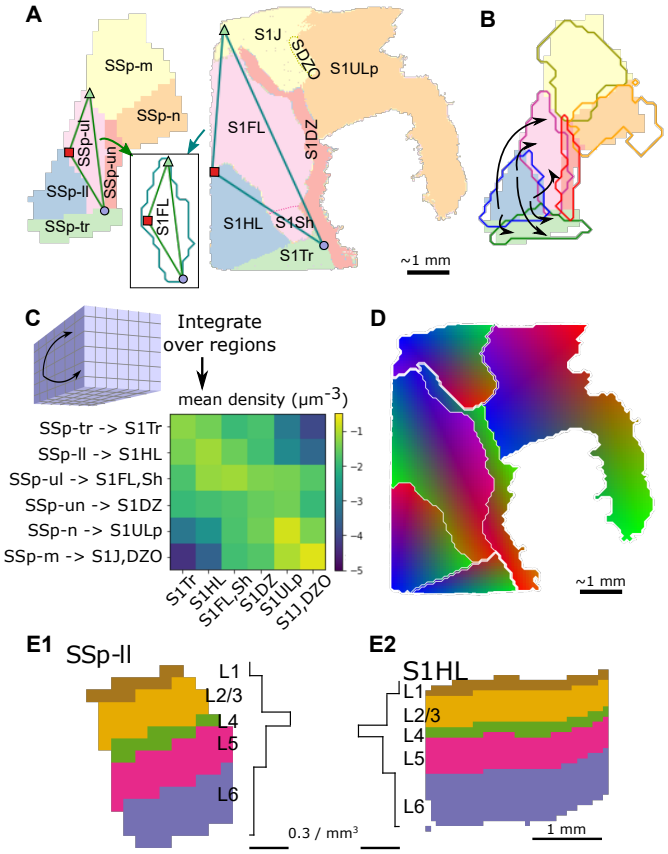

Figure S2: Data sources for connectivity modeling. A: Mapping from mouse to equivalent rat subregions. Left: flat view of mouse somatosensory subregions, Right: equivalent flat view for rat. Corresponding subregions are indicated with matching colors. Triangles are drawn on top of each subregion (shown for SSp-ul and S1FL) using manually annotated points that are assumed to correspond to each other. Inset: These triangles define affine transformations between mouse and rat subregions. B: Transformed rat subregions (colored outlines) are shown overlaid to their corresponding mouse subregions (colored areas). The topographical mapping of connections between subregions predicted in Reimann et al. (2019) (black arrows) can thus be generalized to rat connectivity. C: Mean connection densities between rat somatosensory subregions were derived from the Allen Mouse Brain Connectivity Atlas by summing over corresponding mouse somatosensory subregions. Labels on the left side of the connection density matrix describe the mapping applied from mouse to rat subregions. D: Generalized topographical mapping resulting from the process illustrated in B. Equally colored points are predicted to predominately connect to each other. E: Similarly, predicted layer profiles of connections between subregions (Reimann et al., 2019) are generalized from mouse (E1) to rat (E2).

bioRxiv preprint doi: https://doi.org/10.1101/2022.08.11.503144; this version posted July 29, 2023. The copyright holder for this preprint (which was not certified by peer review) is the author/funder, who has granted bioRxiv a license to display the preprint in perpetuity. It is made available under aCC-BY-NC 4.0 International license.

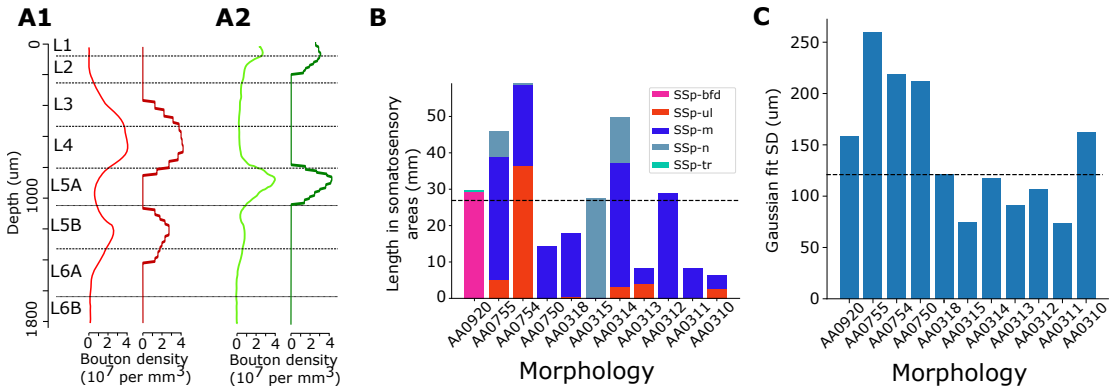

Figure S3: Input data for the derivation of the locations of thalamic inputs. A1: Layer profile of bouton densities of VPM axons in the rat barrel field. Light red: Digitized from Meyer et al. (2010). Dark red: Binned into 20 bins per peak with a lower cutoff of $1/mm^3$ applied. A2: Same for POm axons. B: Total length of 11 reconstructed axons of Janelia MouseLight neurons with somas in VPM in various somatosensory subregions. Dashed line: Median C: Standard deviation of a Gaussian fit of the reconstruction points of the same axons around their centroid in somatosensory areas. Dashed line: Median

Table S2: Normalized depths used for layer boundaries

Boundary		nrmlz. depth
Layer 1	top	0
	bottom	0.079
Layer 2	top	
	bottom	0.151
Layer 3	top	
	bottom	0.32
Layer 4	top	
	bottom	0.411
Layer 5	top	
	bottom	0.664
Layer 6	top	
	bottom	1.0

bioRxiv preprint doi: https://doi.org/10.1101/2022.08.11.503144; this version posted July 29, 2023. The copyright holder for this preprint (which was not certified by peer review) is the author/funder, who has granted bioRxiv a license to display the preprint in perpetuity. It is made available under aCC-BY-NC 4.0 International license.

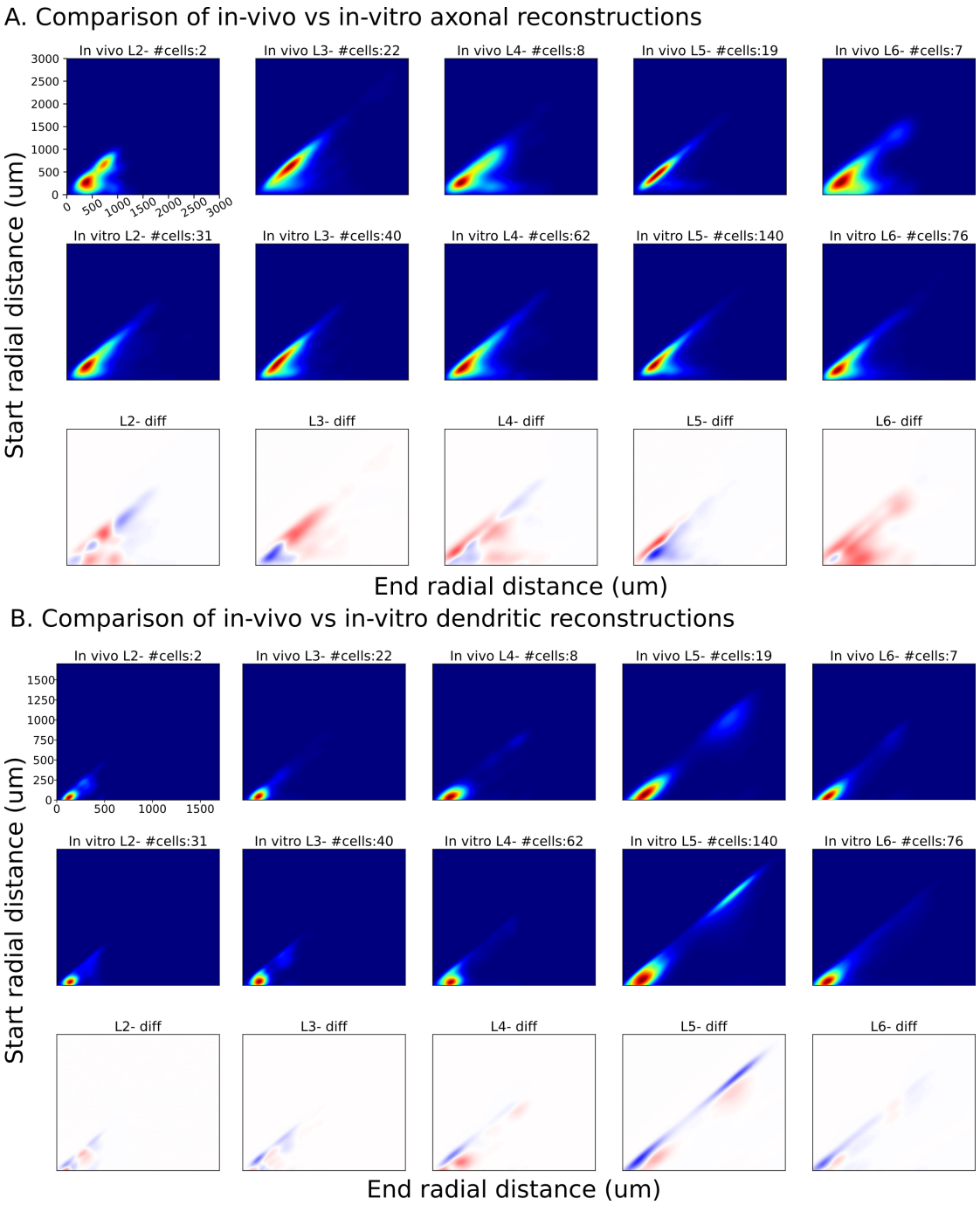

Figure S4: Topological comparison as in (Kanari et al., 2018, 2019) of in-vivo and in-vitro (i.e., from slices) axonal (A) and dendritic (B) reconstructions of rat somatosensory cortex of pyramidal cells from layers 2-6. Top row presents the topological profiles of in-vivo reconstructions, second row presents the topological profiles of in-vitro reconstructions and bottom row the difference between them (red: in-vivo, blue: in-vitro). Number of cells per layer are reported in individual pannels.

bioRxiv preprint doi: https://doi.org/10.1101/2022.08.11.503144; this version posted July 29, 2023. The copyright holder for this preprint (which was not certified by peer review) is the author/funder, who has granted bioRxiv a license to display the preprint in perpetuity. It is made available under aCC-BY-NC 4.0 International license.

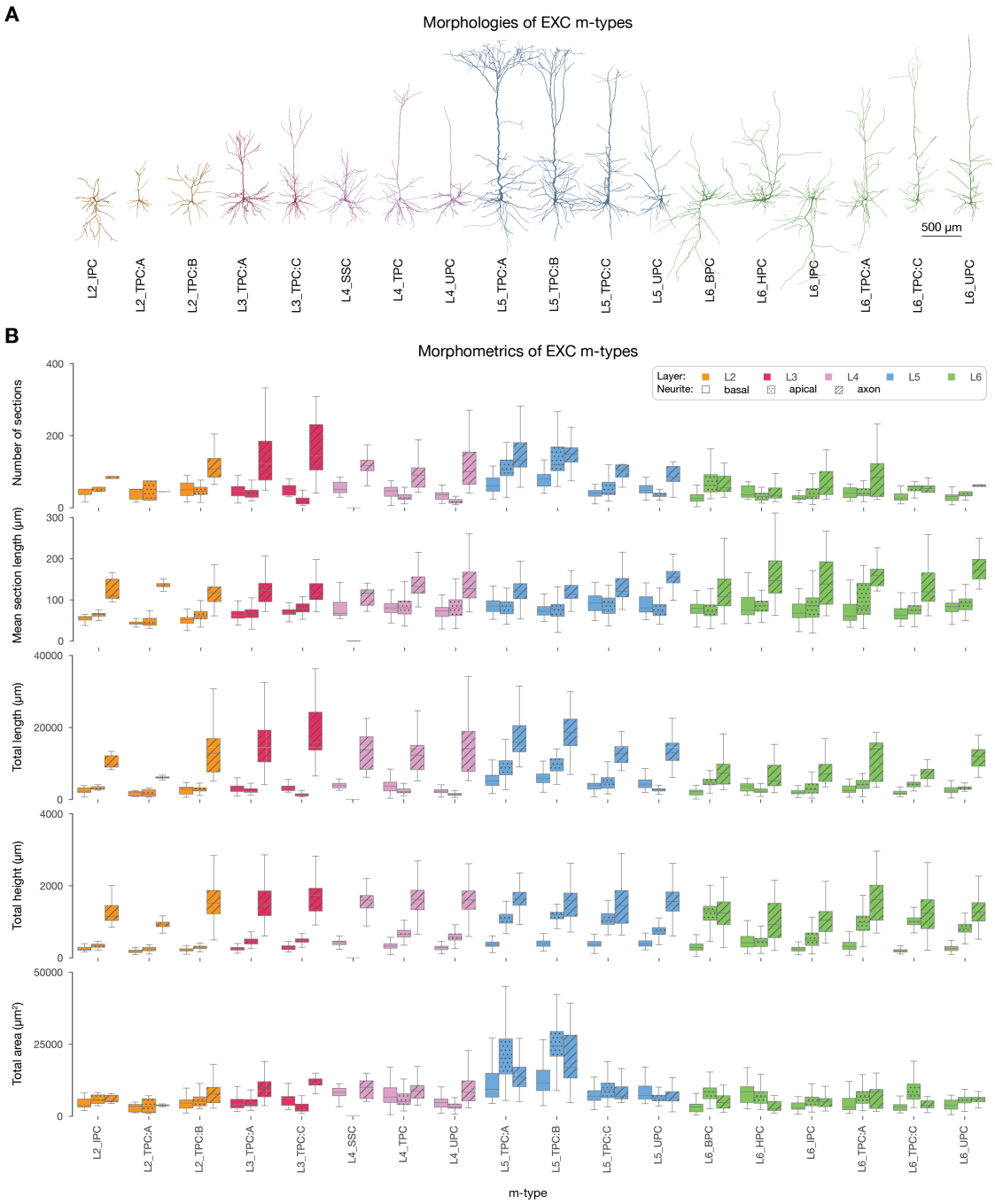

Figure S5: Classification and morphometrics of excitatory morphologies. A: Exemplar 3D reconstructions of the 18 excitatory m-types. Rendering and visualization was done in NeuroMorphoVis (Abdellah et al., 2018). Dendritic diameters are scaled (x3) for better resolution. B: Morphometrics of all morphologies belonging to the 18 excitatory m-types.

bioRxiv preprint doi: https://doi.org/10.1101/2022.08.11.503144; this version posted July 29, 2023. The copyright holder for this preprint (which was not certified by peer review) is the author/funder, who has granted bioRxiv a license to display the preprint in perpetuity. It is made available under aCC-BY-NC 4.0 International license.

Table S3: Placement features used for modeling. The right column denotes the vertical target interval by specifying a layer and a relative offset within the layer, with 0.0 indication the bottom and 1.0 the top of the layer.

L1_HAC	axon	[I:0.00; I:1.00]
L23_MC	axon	[I:0.00; I:1.00]
L2_TPC	axon	[V:0.00; V:1.00]
		[IV:0.00; IV:1.00]
	dendrite	[I:0.00; I:1.00]
L2_TPC:A	axon	[V:0.00; V:1.00]
		[IV:0.00; IV:1.00]
	dendrite	[I:0.00; I:1.00]
L2_TPC:B	axon	[V:0.00; V:1.00]
		[IV:0.00; IV:1.00]
	dendrite	[I:0.00; I:1.00]
L3_TPC	axon	[V:0.00; V:1.00]
		[IV:0.00; IV:1.00]
	dendrite	[I:0.00; I:1.00]
L3_TPC:A	axon	[V:0.00; V:1.00]
		[IV:0.00; IV:1.00]
	dendrite	[I:0.00; I:1.00]
L3_TPC:B	axon	[V:0.00; V:1.00]
		[IV:0.00; IV:1.00]
	dendrite	[I:0.00; I:1.00]
L3_TPC:C	axon	[V:0.00; V:1.00]
		[IV:0.00; IV:1.00]
	dendrite	[I:0.00; I:1.00]
L4_MC	axon	[I:0.00; I:1.00]
L4_SSC	axon	[II:0.00; I:1.00]
L4_TPC	dendrite	[II:0.00; I:1.00]
L4_UPC	dendrite	[II:0.00; I:1.00]
L5_MC	axon	[I:0.00; I:1.00]
		[IV:0.00; IV:1.00]
L5_TPC	axon	[I:0.00; I:1.00]
	dendrite	[I:0.00; I:1.00]
L5_TPC:A	axon	[I:0.00; I:1.00]
	dendrite	[I:0.00; I:1.00]
L5_TPC:B	axon	[I:0.00; I:1.00]
	dendrite	[I:0.00; I:1.00]
L5_TPC:C	axon	[I:0.00; I:1.00]
	dendrite	[I:0.00; I:1.00]
L5_UPC	axon	[I:0.00; I:1.00]
L6_BPC	dendrite	[V:0.50; III:0.10]
L6_HPC	dendrite	[VI:0.00; VI:1.00]
L6_IPC	dendrite	[VI:0.00; V:0.20]
L6_MC	axon	[II:0.00; I:1.00]
		[IV:0.00; IV:1.00]
L6_TPC	dendrite	[V:0.80; III:0.50]
L6_TPC:A	dendrite	[V:0.80; III:0.50]
L6_TPC:C	dendrite	[V:0.80; III:0.50]
L6_UPC	dendrite	[V:0.70; III:0.50]

bioRxiv preprint doi: https://doi.org/10.1101/2022.08.11.503144; this version posted July 29, 2023. The copyright holder for this preprint (which was not certified by peer review) is the author/funder, who has granted bioRxiv a license to display the preprint in perpetuity. It is made available under aCC-BY-NC 4.0 International license.

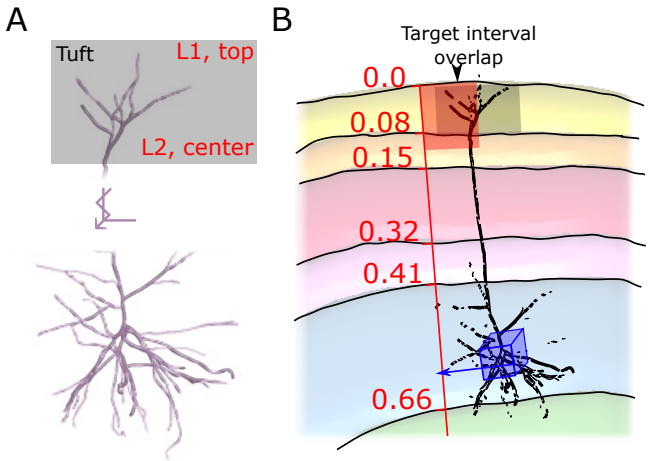

Figure S6: Scoring the placement of a neuron morphology for a voxel. A: Neurite features, here the apical tuft, were manually given a vertical *annotation interval* (grey) and assigned a *target interval*, expressed as a layer interval (red). (Note: parts of the apical dendrite visually shortened.) B: Then the placement of a neuron morphology in a given voxel (blue) is scored as follows: Normalized depth values of the *target interval* are calculated (red); the normalized depth of the voxel is looked up in an atlas (blue); it is used to calculate the normalized depth of the *annotation interval* when the morphology is placed in the voxel (grey); a score is calculated as in (Markram et al., 2015) based on the overlap of the intervals.

Table S4: Number of thalamic fibers providing inputs to the model and each of its subregions.

Subregion	**Number of thalamic input fibers**	
	Core-type	Matrix-type
All	100000	72950
S1ULp	29701	21667
S1FL	25561	18647
S1J	15895	11596
S1HL	12154	8866
S1DZ	7962	5808
S1Tr	5326	3885
S1Sh	1991	1452
S1DZO	1410	1029

bioRxiv preprint doi: https://doi.org/10.1101/2022.08.11.503144; this version posted July 29, 2023. The copyright holder for this preprint (which was not certified by peer review) is the author/funder, who has granted bioRxiv a license to display the preprint in perpetuity. It is made available under aCC-BY-NC 4.0 International license.

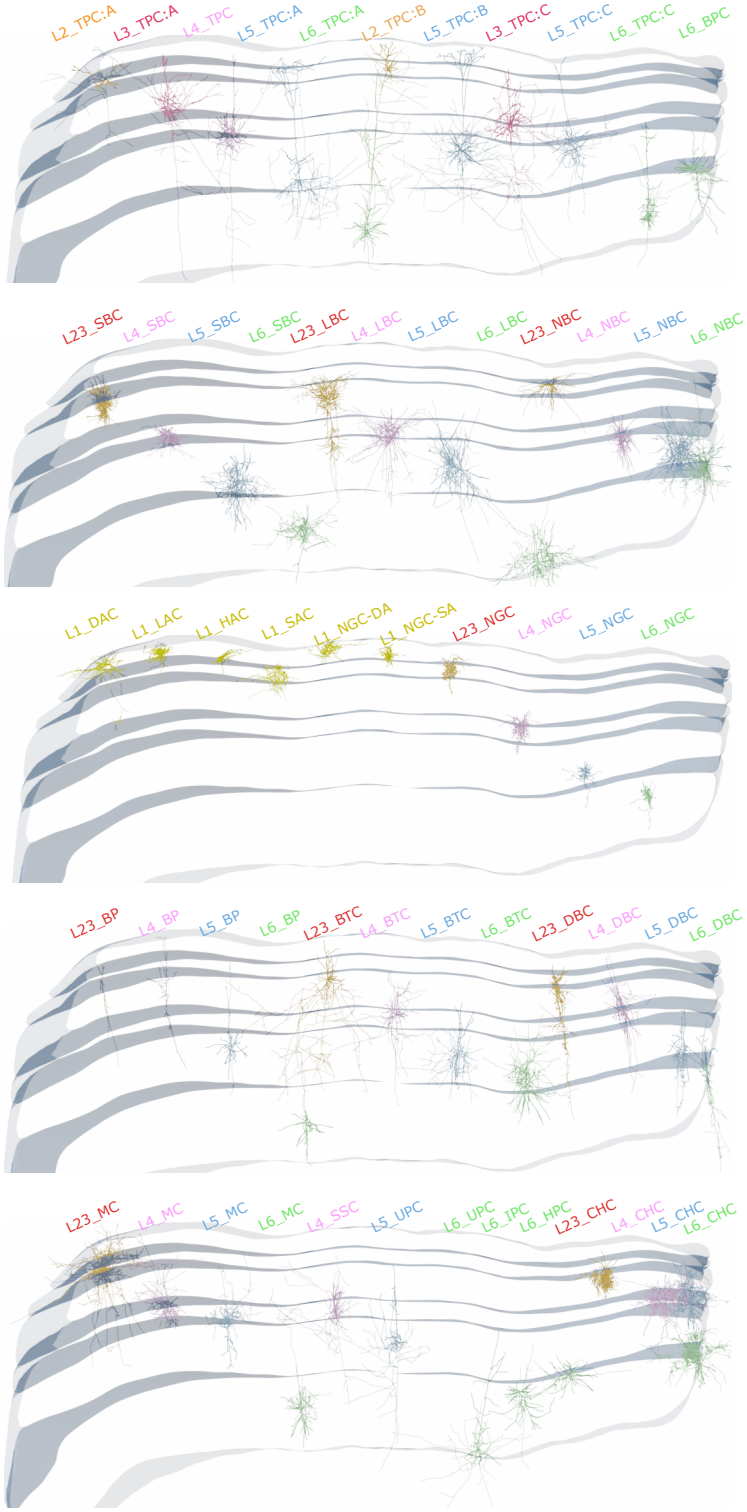

Figure S7: Exemplary neurons in the model, one per m-type, rendered in the context of a slice spanning all cortical layers (grey borders).

bioRxiv preprint doi: https://doi.org/10.1101/2022.08.11.503144; this version posted July 29, 2023. The copyright holder for this preprint (which was not certified by peer review) is the author/funder, who has granted bioRxiv a license to display the preprint in perpetuity. It is made available under aCC-BY-NC 4.0 International license.

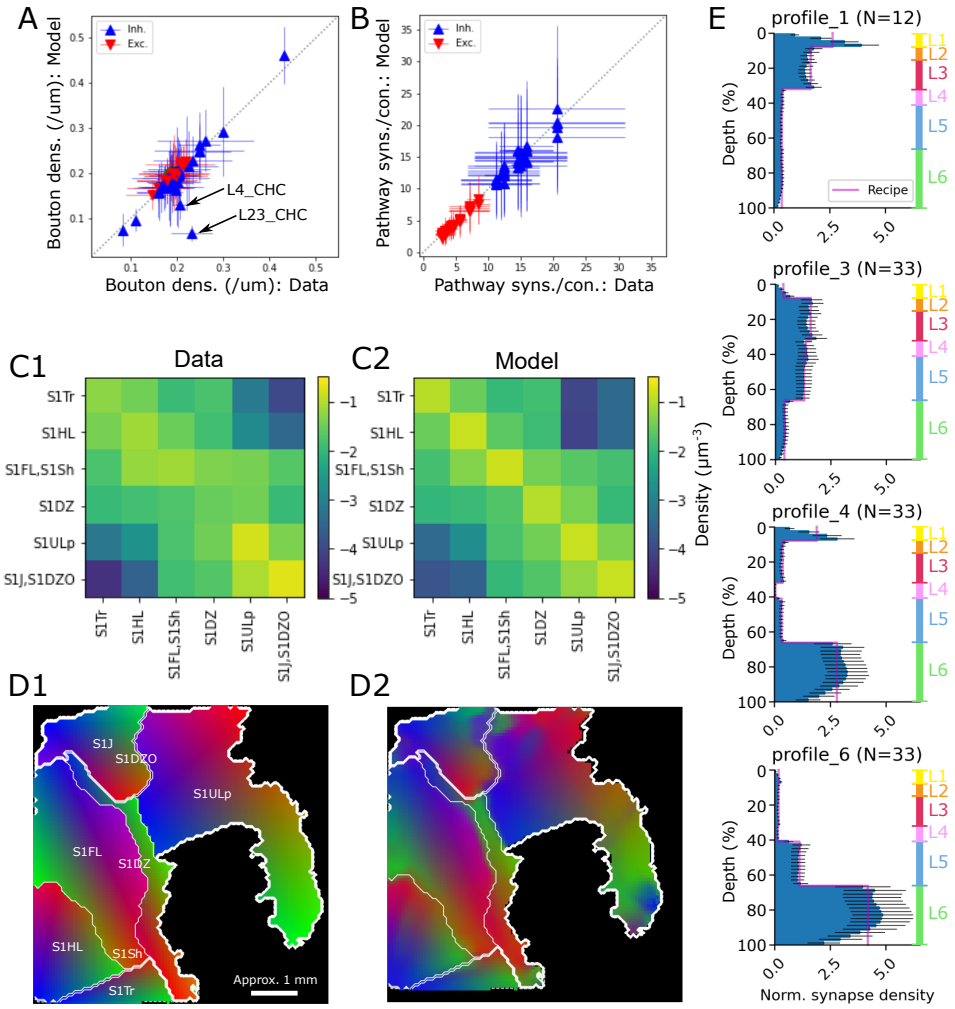

Figure S8: Validation of modeled connectivity. A, B: Touch connectivity is validated by comparing emerging bouton densities (A) and mean numbers of synapses per connection (B) to the target values from the data. Each data point depicts a single morphological type (A) or type-specific pathway (B). Black arrows: Bouton density for Chandelier Cells (ChC) in layers 2, 3 and 4. C: Mean densities of synapses from the union of touch connectivity and long-range connectivity in pathways within and between regions (C2) compared to that target values from the data (C1). D: Structure of the topographical mapping of connections; each part of the model predominately connects to neurons at equally colored locations. (D1) Target mapping from the data. (D2) Analyzed in the union of touch connectivity and long-range connectivity. E: Layer profiles of synapses placed in long-range connections between regions (blue bars) compared to the predicted target profiles from (Reimann et al. (2019), pink lines). Depicted is the density of synapses in a depth bin relative to the overall mean density over the entire depth.

bioRxiv preprint doi: https://doi.org/10.1101/2022.08.11.503144; this version posted July 29, 2023. The copyright holder for this preprint (which was not certified by peer review) is the author/funder, who has granted bioRxiv a license to display the preprint in perpetuity. It is made available under aCC-BY-NC 4.0 International license.

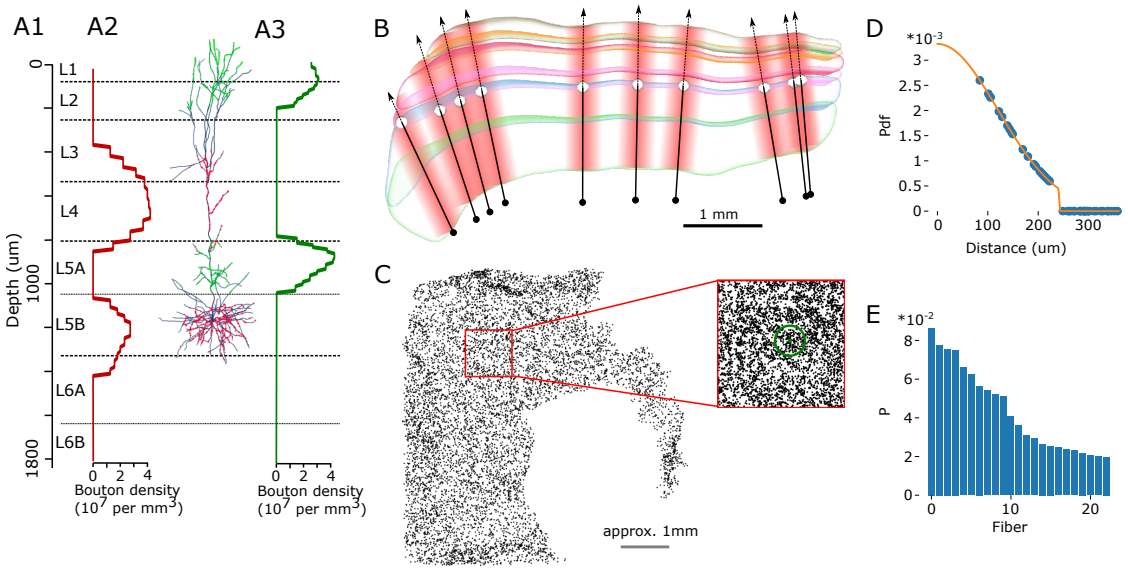

Figure S9: Modeling thalamo-cortical synaptic inputs. A: Input vertical profiles of thalamo-cortical synapses from core-type projections (A1) and matrix-type projections (A3). A2: Exemplary model neuron with projection synapses placed on dendrites according to the prescribed densities. B: Modeling of afferent thalamic fiber locations: Depicted is an exemplary slice of the model. For each fiber a location at the border between layers 4 and 5 is randomly chosen (10 examples shown; white spheres). A point $1500\mu m$ towards the bottom of layer 6 is chosen as the starting point of each fiber (black dots). A domain of influence is then assigned around a line starting at that location with the indicated direction (black arrows and red areas). Influence weakens with distance from the line with a Gaussian profile; for details, see D, E. C: Locations of fibers in the flat view. 10% of the full density shown. Inset: Locations of approximately $1mm^2$ shown in full density. The green circle indicates a single standard deviation of the Gaussian of influence strength used for the core style projections (i.e., $120\mu m$). D: For an exemplary synapse its distances to surrounding fibers is measured and the value of the Gaussian for those distances calculated. It is cut off at two standard deviations. E: The probability that a given fiber is chosen as innervator of a synaptic location (blue bar) is proportional to its value in D (shown only for fibers with nonzero probability).

bioRxiv preprint doi: https://doi.org/10.1101/2022.08.11.503144; this version posted July 29, 2023. The copyright holder for this preprint (which was not certified by peer review) is the author/funder, who has granted bioRxiv a license to display the preprint in perpetuity. It is made available under aCC-BY-NC 4.0 International license.

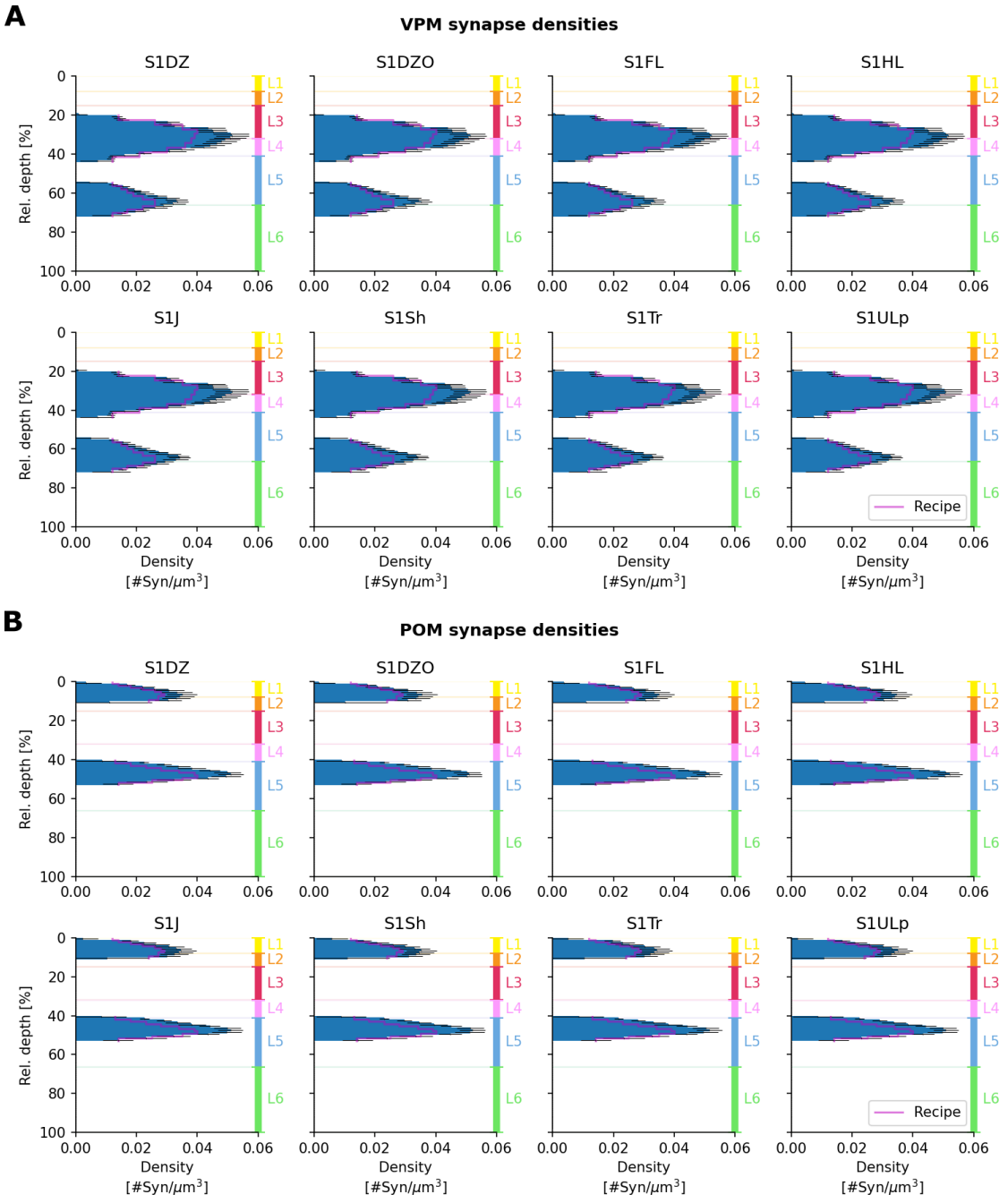

Figure S10: Validation of thalamo-cortical density profiles. Synapse density profiles of thalamo-cortical synapses from core-type (VPM) projections (A) and matrix-type (POm) projections (B), compared with the target profiles from Meyer et al. (2010) (pink lines). Depicted are the mean densities (black lines: ± SD) over voxels within depth bins relative to the respective total cortical thickness in each of the eight sub-regions.

bioRxiv preprint doi: https://doi.org/10.1101/2022.08.11.503144; this version posted July 29, 2023. The copyright holder for this preprint (which was not certified by peer review) is the author/funder, who has granted bioRxiv a license to display the preprint in perpetuity. It is made available under aCC-BY-NC 4.0 International license.

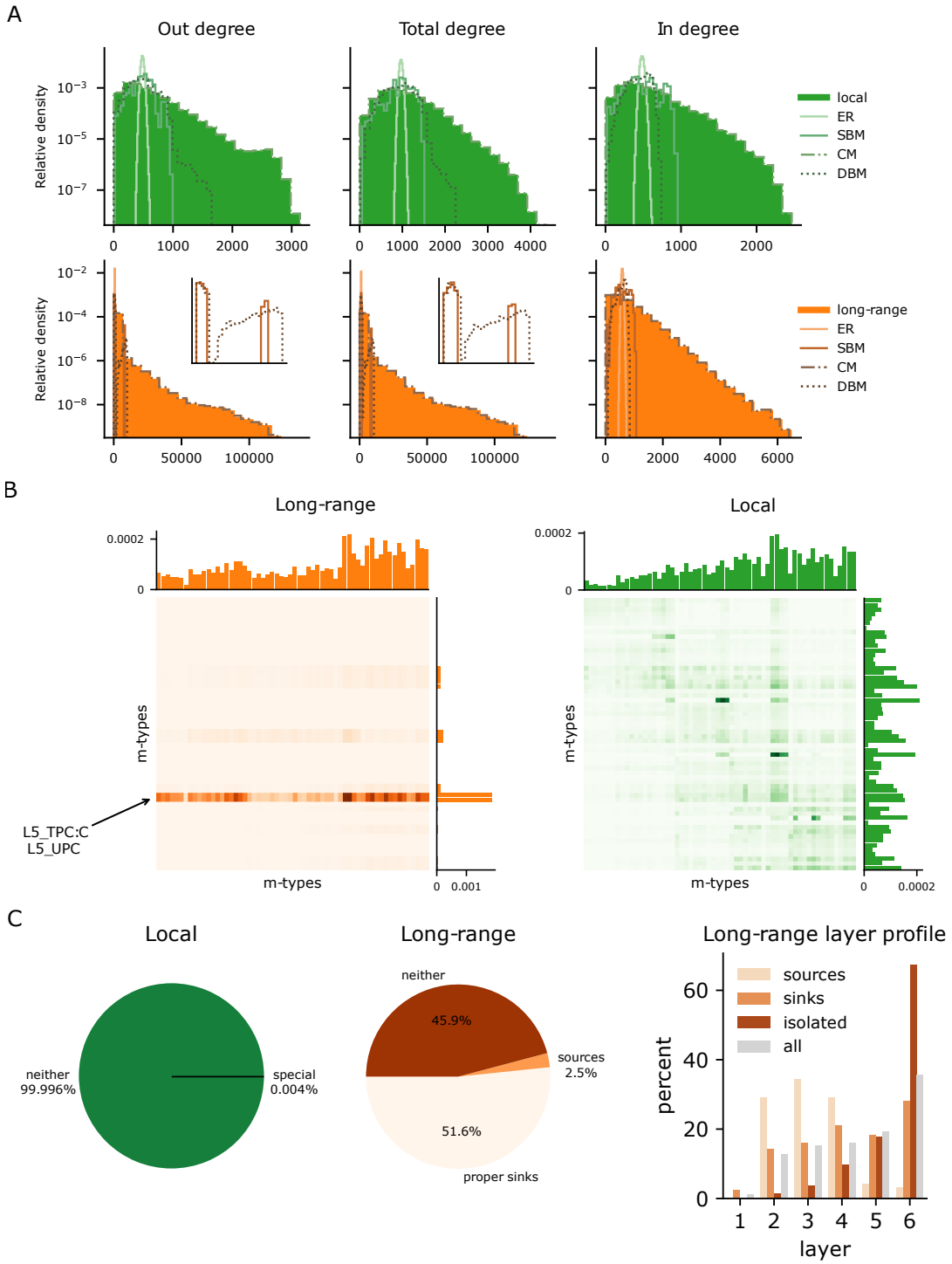

Figure S11: Basic properties of network connectivity. A:Top/bottom degree distributions of the local/long-range networks and their corresponding control models. On the second row additional inserts are provided showing the bi-modality of the out and total degree distributions of the SBM and DBM controls. B: Matrices showing the probability of connection between given pre/post-synpatic m-types. Vertically at the right of each matrix the probability of connection for a fixed pre-synaptic m-type. Horizontally on top of each matrix, the probability of connection for a fixed post-synaptic m-type. C: Left and center, percentage of special nodes in both networks, sources (nodes of in-degree 0) and proper sinks (nodes of out-degree 0 that are not isolated nodes). Left: layer distribution of the special nodes of the long-range network.

bioRxiv preprint doi: https://doi.org/10.1101/2022.08.11.503144; this version posted July 29, 2023. The copyright holder for this preprint (which was not certified by peer review) is the author/funder, who has granted bioRxiv a license to display the preprint in perpetuity. It is made available under aCC-BY-NC 4.0 International license.

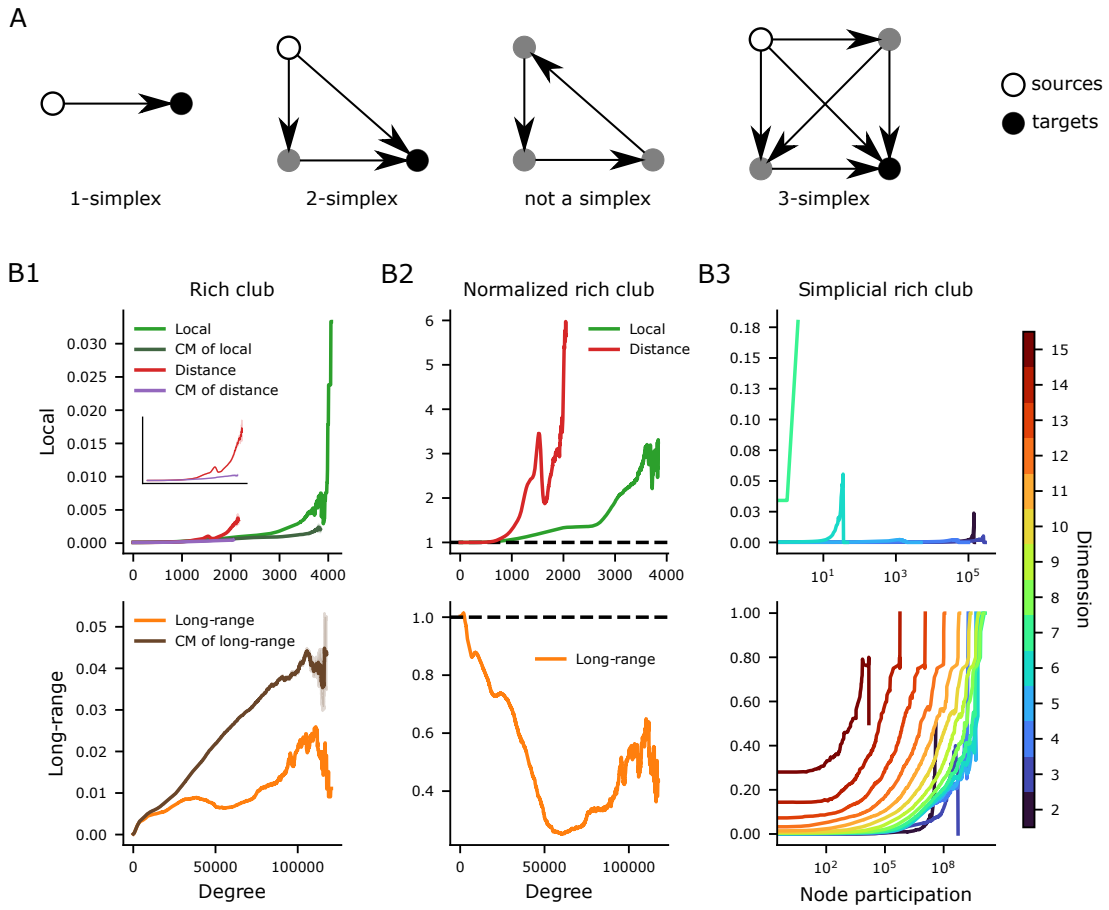

Figure S12: Rich club analysis A: Depiction of simplices and non-simplices in various dimensions with distinction between the source and target nodes. B:Rich-club analysis, top/bottom rows for the local/long-range networks. Left column, rich-club curves for the original networks as well as their CM controls. Top left additionally shows the rich-club curves of the DBM controls of the local-networks as well as their corresponding CM controls. Middle column shows normalized rich club curves obtained by dividing the rich-club curves for the original networks by the mean of the rich-club curves of their corresponding controls. Right column shows the simplicial rich club curves for color-coded dimensions ≥ 2.